

¹ A novel inf-sup-based volumetric constraint ratio and
² its implementation via mixed FE-meshfree formulation

³ Junchao Wu^{a,*}, Yingjie Chu^b, Yangtao Xu^a

^a Key Laboratory for Intelligent Infrastructure and Monitoring of Fujian Province, College
of Civil Engineering, Huaqiao University, Xiamen, Fujian, 361021, China

^b Fujian Key Laboratory of Digital Simulations for Coastal Civil Engineering, Department
of Civil Engineering, Xiamen University, Xiamen, Fujian, 361005, China

⁴ **Abstract**

Numerical formulations for incompressible materials often suffer from volumetric locking, which reduces the accuracy of displacement solutions and introduces oscillations in the pressure field. A well-chosen constraint ratio can mitigate this issue, but traditional approaches lack a theoretical foundation based on the inf-sup (or LBB) condition, which is essential for the stability of mixed formulations. This paper introduces a novel optimal constraint ratio derived from the inf-sup condition to address volumetric locking. The inf-sup test, a numerical tool for verifying the inf-sup condition, is reaffirmed to be equivalent to the inf-sup condition through a variational approach. By incorporating a complete polynomial space whose dimension matches the number of displacement degrees of freedom (DOFs), a new inf-sup value estimator is developed, explicitly considering the constraint ratio. For a given number of displacement DOFs, when the pressure DOFs of a numerical formulation remain below a stabilized number that falls into the optimal constraint ratio range, this numerical formulation actually satisfies the inf-sup condition. To implement the optimal constraint ratio, a mixed finite element and meshfree formulation is proposed, where displacements are discretized using traditional finite element approximations, and pressures are approximated via the reproducing kernel meshfree method. Leveraging the globally smooth reproducing kernel shape functions, the constraint ratio can be flexibly adjusted to meet the inf-sup condition without the limit of element. For computational efficiency and ease of implementation, pressure nodes are placed on selected displacement nodes to maintain the optimal constraint ratio. Inf-sup tests and a series of 2D and 3D incompressible elasticity examples validate the proposed constraint ratio, demonstrating its effectiveness in eliminating volumetric locking and enhancing the performance of mixed finite element and meshfree formulations.

⁵ **Keywords:** Optimal constraint ratio, Inf-sup condition estimator, Volumetric
⁶ locking, Mixed formulation, Reproducing kernel meshfree approximation

^{*}Corresponding author

Email address: jcwu@hqu.edu.cn (Junchao Wu)
Preprint submitted to Elsevier

September 7, 2025

7 **1. Introduction**

8 The volumetric constraint is a necessary condition in the numerical formulation
 9 of incompressible materials like rubber and hydrogel. Proper imposition of
 10 this constraint is crucial for obtaining better numerical solutions; insufficient or
 11 excessive constraints will reduce the accuracy and stability of the solution [1].
 12 The volumetric constraint ratio [2], denoted as r , is often used to measure the
 13 level of constraint. It is defined as the total degrees of freedom (DOFs) of dis-
 14 placement divided by the total DOFs of pressure. Ideally, the optimal constraint
 15 ratio should be consistent with its governing partial differential equations. For
 16 example, in the two-dimensional (2D) case, the optimal constraint ratio is 2,
 17 since there are two governing equations for displacement and one for pressure.
 18 When the constraint ratio is less than 2, the formulation suffers from volumetric
 19 locking, while a constraint ratio greater than 2 can cause a coarse solution for
 20 pressure. These observations have been summarized as follows[2]:

$$r = \frac{2n_u}{n_p}, \quad \begin{cases} r > 2 & \text{too few constraints} \\ r = 2 & \text{optimal} \\ r < 2 & \text{too many constraints} \\ r \leq 1 & \text{severe locking} \end{cases} \quad (1)$$

21 where n_u and n_p are the numbers of control nodes for displacement and pressure,
 22 respectively. Classifying the locked status via the constraint ratio is straight-
 23 forward but imprecise. For instance, the constraint ratio can remain 2 while
 24 the pressure is discretized using continuous shape functions identical to the
 25 displacement's approximation. However, volumetric locking still exists in this
 26 formulation [2].

27 The inf-sup condition, also known as the Ladyzhenskay–Babuška–Brezzi
 28 (LBB) condition [3, 4], is a more precise requirement for a locking-free for-
 29 mulation. This condition is based on the mixed formulation framework, and
 30 when the inf-sup condition is satisfied, both the accuracy and stability of the
 31 mixed-formulation can be ensured. However, verifying the inf-sup condition is
 32 non-trivial. An eigenvalue problem namely inf-sup test can be used to check
 33 this condition numerically [5, 6, 7, 8]. Analytically, Brezzi and Fortin proposed
 34 a two-level projection framework that always satisfies the inf-sup condition, al-
 35 lowing it to be checked by identifying whether the formulation is included in
 36 this framework. Both analytical and numerical methods to check the inf-sup
 37 condition are complex, and the relationship between the constraint ratio and
 38 the inf-sup condition remains unclear.

39 To address volumetric constraint issues, adjusting the constraint ratio to an
 40 appropriate level is commonly used and easily implemented. In traditional finite
 41 element methods (FEM), this adjustment is carried out based on elements since
 42 the DOFs are embedded in each element. Conventional FEM often exhibits
 43 an over-constrained status. Reducing the approximation order of pressure in
 44 mixed formulation can alleviate the constraint burden, such as with the well-
 45 known Q4P1 (4-node quadrilateral displacement element with 1-node piecewise

constant pressure element) and Q8P3. Globally, using continuous shape functions to link the local pressure DOFs in each element can also reduce the total number of pressure DOFs and increase the constraint ratio, such as with T6C3 (6-node triangular displacement element with 3-node continuous linear pressure element) and Q9C4 (Taylor–Hood element) [9]. These schemes belong to the mixed formulation framework and can also be implemented through a projection approach, where the pressure approximant is projected into a lower-dimensional space. Examples include selective integration methods [10, 11], B–bar or F–bar methods [12, 13, 14, 15], pressure projection methods [16, 17, 18, 19, 20], and enhanced strain method [21]. Meanwhile, conventional 3-node triangular elements arranged in a regular cross pattern can also reduce the dimension of the pressure space [22]. It should be noted that not all of these methods meet the inf–sup condition despite alleviating volumetric locking and producing a good displacement solution. Some methods, like Q4P1, show significant oscillation for the pressure solution, known as spurious pressure mode or checkerboard mode [22]. In such cases, additional stabilization approaches, such as variational multi-scale stabilization (VMS) [23, 24, 25, 26, 27], Galerkin/least-squares (GLS) [28], or Streamline upwind/Petrov–Galerkin formulation (SUPG) [29, 30] are required to eliminate the oscillations in pressure.

Another class of FEM methods adjusts the constraint ratio by increasing the displacement DOFs. For instance, based on 3-node triangular elements, Arnold et al. [31, 32] used a cubic bubble function in each element to increase the displacement DOFs, known as the MINI element. It has been shown that this method belongs to the VMS framework [33], and its fulfillment of the inf–sup condition can be analytically evidenced using the two-level projection framework [7]. The Crouzeix–Raviart element [34] transfers the DOFs from the triangular vertices to edges, increasing the constraint ratio since, for triangular topology, the number of edges is greater than that of vertices. More details about FEM technology for volumetric constraint issues can be found in Refs. [2, 4, 35].

In the past two decades, various novel approximations equipped with globally smooth shape functions, such as moving least-squares approximation [36], reproducing kernel approximation [37, 38], radial basis functions [39, 40], maximum-entropy approximation [41], and NURBS approximation [42, 43], have been proposed. In these approaches, the approximant pressure evaluated by the derivatives of globally continuous shape functions also maintains a constraint ratio of 2 in 2D incompressible elasticity problems. However, the corresponding results still show lower accuracy caused by locking [44, 45]. Widely-used locking-free technologies for FEM are introduced in these approaches to enhance their performance. For example, Moutsanidis et al. [46, 47] employed selective integration and B–bar, F–bar methods for reproducing kernel particle methods. Wang et al. [48] applied selective integration schemes with bubble-stabilized functions to node-based smoothed particle FEM. Elguedj et al. [49] proposed the B–bar and F–bar NURBS formulations for linear and nonlinear incompressible elasticity. Chen et al. [50] adopted the pressure projection approach for reproducing kernel formulations for nearly-incompressible problems, which was later extended

to Stokes flow formulations by Goh et al. [51]. Bombarde et al. [52] developed a block-wise NURBS formulation for shell structures, eliminating locking via pressure projection. Casquero and Golestanian [53] proposed a NURBS-based continuous-assumed-strain element to alleviate volumetric locking. Most of these approximations offer better flexibility for arranging DOFs since their shape function constructions are no longer element-dependent. Huerta et al.[54] proposed a reproducing kernel approximation with divergence-free basis functions to avoid volumetric strain entirely , although this approach is unsuitable for compressible cases. Wu et al. [55] added extra displacement DOFs in FEM elements to resolve the locking issue, constructing local shape functions using generalized meshfree interpolation to maintain consistency. Vu-Huu et al. [56] employed different-order polygonal finite element shape functions to approximate displacement and pressure, embedding a bubble function in each element for stabilization.

This work proposes a more precise optimal volumetric constraint ratio and implements a locking-free mixed FE-meshfree formulation with this optimal constraint ratio. Firstly, the inf-sup condition is derived in a new form, showing that the inf-sup value equals to the lowest non-zero eigenvalue of dilatation stiffness in the context of variational analysis. Subsequently, involving a complete polynomial space with dimensions identical to displacement DOFs, the number of non-zero eigenvalues can be analytically calculated, and a new estimator considering the constraint ratio is established. From this estimator, the optimal constraint ratio is defined with a stabilized number of pressure nodes. If the constraint ratio exceeds the locking ratio, the formulation will show severe locking. When the constraint ratio is lower than the optimal ratio, the formulation achieves satisfactory results, and the inf-sup condition is fulfilled. This estimator provides a strong link between the inf-sup value and the pressure DOFs, making it possible to justify the locking status by counting the pressure nodes. Furthermore, a mixed FE-meshfree formulation is proposed to verify the optimal constraint ratio. In this mixed formulation, the displacement is approximated by traditional finite element methods, and the pressure is discretized by reproducing kernel meshfree approximation. With the aid of global RK shape functions, the pressure's DOFs can be adjusted arbitrarily without considering approximation order and numerical integration issues to maintaining the constraint ratio as optimal.

The remainder of this paper is organized as follows: Section 2 reviews the mixed formulation framework for incompressible elasticity problems. In Section 3, a novel estimator of the inf-sup value is developed, from which the optimal constraint ratio is obtained. Section 4 introduces the mixed FE-meshfree formulation and its corresponding nodal distribution schemes. Section 5 verifies the proposed optimal constraint ratio using a set of benchmark incompressible elasticity examples, studying error convergence and stability property for the mixed FE-meshfree approximation. Finally, the conclusions are presented in Section 6.

¹³⁶ **2. Mixed-formulation**

¹³⁷ *2.1. Nearly-incompressible elasticity*

¹³⁸ Consider a body $\Omega \in \mathbb{R}^{n_d}$ with boundary Γ in n_d -dimension, where Γ_t and
¹³⁹ Γ_g denote its natural boundary and essential boundary, respectively, such that
¹⁴⁰ $\Gamma_t \cup \Gamma_g = \Gamma$, $\Gamma_t \cap \Gamma_g = \emptyset$. The corresponding governing equations for the mixed
¹⁴¹ formulation are given by:

$$\begin{cases} \nabla \cdot \boldsymbol{\sigma} + \mathbf{b} = \mathbf{0} & \text{in } \Omega \\ \frac{p}{\kappa} + \nabla \cdot \mathbf{u} = 0 & \text{in } \Omega \\ \boldsymbol{\sigma} \cdot \mathbf{n} = \mathbf{t} & \text{on } \Gamma_t \\ \mathbf{u} = \mathbf{g} & \text{on } \Gamma_g \end{cases} \quad (2)$$

¹⁴² where \mathbf{b} denotes the prescribed body force in Ω . \mathbf{t}, \mathbf{g} are prescribed traction and
¹⁴³ displacement on natural and essential boundaries, respectively. \mathbf{u} and p , standing
¹⁴⁴ for displacement and hydrostatic pressure, respectively, are the variables of
¹⁴⁵ this problem. ∇ is the gradient tensor defined by $\nabla = \frac{\partial}{\partial x_i} \mathbf{e}_i$. $\boldsymbol{\sigma}$ denotes the
¹⁴⁶ stress tensor and has the following form:

$$\boldsymbol{\sigma}(\mathbf{u}, p) = p \mathbf{1} + 2\mu \nabla^d \mathbf{u} \quad (3)$$

¹⁴⁷ in which $\mathbf{1} = \delta_{ij} \mathbf{e}_i \otimes \mathbf{e}_j$ is the second-order identity tensor. $\nabla^d \mathbf{u}$ is the deviatoric
¹⁴⁸ gradient of \mathbf{u} and can be evaluated by:

$$\nabla^d \mathbf{u} = \frac{1}{2} (\mathbf{u} \nabla + \nabla \mathbf{u}) - \left(\frac{1}{3} \nabla \cdot \mathbf{u} \right) \mathbf{1} \quad (4)$$

¹⁴⁹ and κ, μ are the bulk modulus and shear modulus, respectively, and they can
¹⁵⁰ be represented by Young's modulus E and Poisson's ratio ν :

$$\kappa = \frac{E}{2(1-2\nu)}, \quad \mu = \frac{E}{3(1+\nu)} \quad (5)$$

¹⁵¹ In accordance with the Galerkin formulation, the weak form can be given
¹⁵² by: Find $\mathbf{u} \in V, p \in Q$, such that

$$\begin{cases} a(\mathbf{v}, \mathbf{u}) + b(\mathbf{v}, p) = f(\mathbf{v}) & \forall \mathbf{v} \in V \\ b(\mathbf{u}, q) + c(q, p) = 0 & \forall q \in Q \end{cases} \quad (6)$$

¹⁵³ with the spaces V, Q defined by:

$$V = \{\mathbf{v} \in H^1(\Omega)^2 \mid \mathbf{v} = \mathbf{g}, \text{ on } \Gamma_g\} \quad (7)$$

$$Q = \{q \in L^2(\Omega) \mid \int_{\Omega} q d\Omega = 0\} \quad (8)$$

¹⁵⁴ where $a : V \times V \rightarrow \mathbb{R}$, $b : V \times Q \rightarrow \mathbb{R}$ and $c : Q \times Q \rightarrow \mathbb{R}$ are bilinear forms,
¹⁵⁵ and $f : V \rightarrow \mathbb{R}$ is the linear form. In elasticity problems, they are given by:

$$a(\mathbf{v}, \mathbf{u}) = \int_{\Omega} \nabla^d \mathbf{v} : \nabla^d \mathbf{u} d\Omega \quad (9)$$

$$b(\mathbf{v}, q) = \int_{\Omega} \nabla \cdot \mathbf{v} q d\Omega \quad (10)$$

$$c(q, p) = - \int_{\Omega} \frac{1}{3\kappa} q p d\Omega \quad (11)$$

$$f(\mathbf{v}) = \int_{\Gamma_t} \mathbf{v} \cdot \mathbf{t} d\Gamma + \int_{\Omega} \mathbf{v} \cdot \mathbf{b} d\Omega \quad (12)$$

¹⁵⁶ *2.2. Ritz–Galerkin problem and volumetric locking*

¹⁵⁷ In the mixed-formulation framework, the displacement and pressure can be
¹⁵⁸ discretized by different approximations. The approximant displacement \mathbf{u}_h and
¹⁵⁹ approximant pressure p_h can be expressed by:

$$\mathbf{u}_h(\mathbf{x}) = \sum_{I=1}^{n_u} N_I(\mathbf{x}) \mathbf{u}_I, \quad p_h(\mathbf{x}) = \sum_{K=1}^{n_p} \Psi_K(\mathbf{x}) p_K \quad (13)$$

¹⁶⁰ where N_I and Ψ_K are the shape functions for the displacement and pressure, \mathbf{u}_I
¹⁶¹ and p_K are the corresponding coefficients. Leading these approximations into
¹⁶² the weak form of Eq. (6) yields the following Ritz–Galerkin problems: Find
¹⁶³ $\mathbf{u}_h \in V_h$, $p_h \in Q_h$, such that

$$\begin{cases} a(\mathbf{v}_h, \mathbf{u}_h) + b(\mathbf{v}_h, p_h) = f(\mathbf{v}_h) & \forall \mathbf{v}_h \in V_h \\ b(\mathbf{u}_h, q_h) + c(q_h, p_h) = 0 & \forall q_h \in Q_h \end{cases} \quad (14)$$

¹⁶⁴ where the spaces $V_h \subseteq V$, $Q_h \subseteq Q$ are defined by:

$$V_h = \{\mathbf{v}_h \in (\text{span}\{N_I\}_{I=1}^{n_u})^{n_d} | \mathbf{v}_h = \mathbf{g}, \text{ on } \Gamma_g\} \quad (15)$$

$$Q_h = \{q_h \in \text{span}\{\Psi_K\}_{K=1}^{n_p} | \int_{\Omega} q_h d\Omega = 0\} \quad (16)$$

¹⁶⁵ For nearly incompressible material, the Poisson ratio approaches 0.5, and
¹⁶⁶ the bulk modulus κ will tend to infinity based on Eq. (5). Then, the bilinear
¹⁶⁷ form c in Eq. (11) tends to zero. And the weak form of Eq. (14) becomes an
¹⁶⁸ enforcement of the volumetric strain $\nabla \cdot \mathbf{u}_h$ to be zero using the Lagrangian
¹⁶⁹ multiplier method, where p_h is the Lagrangian multiplier.

¹⁷⁰ Furthermore, from the second line of Eq. (14), we have:

$$b(\mathbf{u}_h, q_h) + c(q_h, p_h) = (q_h, \nabla \cdot \mathbf{u}_h) - (q_h, \frac{1}{3\kappa} p_h) = 0, \quad \forall q_h \in Q_h \quad (17)$$

¹⁷¹ or

$$(q_h, 3\kappa \nabla \cdot \mathbf{u}_h - p_h) = 0, \quad \forall q_h \in Q_h \quad (18)$$

¹⁷² where (\bullet, \bullet) is the inner product operator evaluated by:

$$(q, p) := \int_{\Omega} q p d\Omega \quad (19)$$

¹⁷³ Obviously, in Eq. (18), p_h is the orthogonal projection of $3\kappa \nabla \cdot \mathbf{u}_h$ with respect
¹⁷⁴ to the space Q_h [1], and, for further development, we use the nabla notation
¹⁷⁵ with an upper tilde to denote the projection operator, i.e., $p_h = \tilde{\nabla} \cdot \mathbf{u}_h$. In this
¹⁷⁶ circumstance, the bilinear form b in the first line of Eq. (14) becomes:

$$\begin{aligned} b(\mathbf{v}_h, p_h) &= (\underbrace{\nabla \cdot \mathbf{v}_h - \tilde{\nabla} \cdot \mathbf{v}_h, p_h}_{0}) + (\tilde{\nabla} \cdot \mathbf{v}_h, \underbrace{p_h}_{3\kappa \tilde{\nabla} \cdot \mathbf{u}_h}) \\ &= (\tilde{\nabla} \cdot \mathbf{v}_h, 3\kappa \tilde{\nabla} \cdot \mathbf{u}_h) \\ &= \tilde{a}(\mathbf{v}_h, \mathbf{u}_h) \end{aligned} \quad (20)$$

¹⁷⁷ where the bilinear form $\tilde{a} : V_h \times V_h \rightarrow \mathbb{R}$ is defined by:

$$\tilde{a}(\mathbf{v}_h, \mathbf{u}_h) = \int_{\Omega} 3\kappa \tilde{\nabla} \cdot \mathbf{v}_h \tilde{\nabla} \cdot \mathbf{u}_h d\Omega \quad (21)$$

¹⁷⁸ Accordingly, the problem of Eq. (14) becomes a one-variable form: Find
¹⁷⁹ $\mathbf{u}_h \in V_h$, such that

$$a(\mathbf{v}_h, \mathbf{u}_h) + \tilde{a}(\mathbf{v}_h, \mathbf{u}_h) = f(\mathbf{v}_h), \quad \forall \mathbf{v}_h \in V_h \quad (22)$$

¹⁸⁰ As $\kappa \rightarrow \infty$, Eq. (22) can be regarded as an enforcement of volumetric strain
¹⁸¹ using the penalty method, where \tilde{a} is the penalty term. However, it should
¹⁸² be noted that, if the mixed-formulation wants to obtain a satisfactory result,
¹⁸³ this orthogonal projection must be surjective [57]. In the case where it is not
¹⁸⁴ surjective, for a given $p_h \in Q_h$, it may not be possible to find a $\mathbf{u}_h \in V_h$ such that
¹⁸⁵ $p_h = 3\kappa \nabla \cdot \mathbf{u}_h$. This will lead to a much smaller displacement than expected and
¹⁸⁶ an oscillated pressure result. This phenomenon is called volumetric locking.

¹⁸⁷ 3. Optimal volumetric constraint ratio

¹⁸⁸ 3.1. Inf-sup condition and its eigenvalue problem

¹⁸⁹ To ensure the surjectivity of orthogonal projection and satisfactory results,
¹⁹⁰ the approximations of Eq.(7) should satisfy the inf-sup condition, also known
¹⁹¹ as the Ladyzhenskaya–Babuška–Brezzi condition [4]:

$$\inf_{q_h \in Q_h} \sup_{\mathbf{v}_h \in V_h} \frac{|b(q_h, \mathbf{v}_h)|}{\|q_h\|_Q \|\mathbf{v}_h\|_V} \geq \beta > 0 \quad (23)$$

¹⁹² in which β , namely the inf-sup value, is a constant independent of the char-
¹⁹³ acterized element size h . The norms $\|\bullet\|_V$ and $\|\bullet\|_Q$ can be flexibly defined

¹⁹⁴ by:

$$\|\mathbf{v}\|_V^2 := \int_{\Omega} \nabla^d \mathbf{v} : \nabla^d \mathbf{v} d\Omega \quad (24)$$

$$\|q\|_Q^2 := \int_{\Omega} \frac{1}{3\kappa} q^2 d\Omega \quad (25)$$

¹⁹⁵ Additionally, the Appendix A lists the displacement and pressure error estimators for the mixed-formulations. This indicates how the inf-sup value β affects ¹⁹⁶ the solution accuracy.

¹⁹⁸ To establish the relationship between the inf-sup condition and the constraint ratio, the inf-sup condition is firstly transformed by the following Lemma ¹⁹⁹ 1:

²⁰¹ **Lemma 1.** Suppose $\mathcal{P}_h : V_h \rightarrow Q_h$ is the orthogonal projection operator of the ²⁰² divergence operator $\mathcal{P} := 3\kappa \nabla \cdot$, i.e., $\mathcal{P}_h := 3\kappa \tilde{\nabla} \cdot$ and satisfies Eq. (18). Then, ²⁰³ the inf-sup value can be estimated by:

$$\beta \leq \inf_{V'_h \subset V_h \setminus \ker \mathcal{P}_h} \sup_{\mathbf{v}_h \in V'_h} \frac{\|\mathcal{P}_h \mathbf{v}_h\|_Q}{\|\mathbf{v}_h\|_V} \quad (26)$$

²⁰⁴ in which $\ker \mathcal{P}_h \subset V_h$ is the kernel of \mathcal{P}_h defined by $\ker \mathcal{P}_h := \{\mathbf{v}_h \in V_h \mid \mathcal{P}_h \mathbf{v}_h = 0\}$.

²⁰⁶ PROOF. First, define the image space of \mathcal{P}_h as $\text{Im} \mathcal{P}_h := \{p_h \in Q_h \mid \exists \mathbf{v}_h \in V_h, p_h = \mathcal{P}_h \mathbf{v}_h\}$. Since $\mathcal{P}_h \subset Q_h$, Eq. (23) can be rewritten as:

$$\begin{aligned} \beta &\leq \inf_{q_h \in Q_h} \sup_{\mathbf{v}_h \in V_h} \frac{|b(q_h, \mathbf{v}_h)|}{\|q_h\|_Q \|\mathbf{v}_h\|_V} = \inf_{q_h \in Q_h} \sup_{\mathbf{v}_h \in V_h} \frac{|(q_h, \frac{1}{3\kappa} \mathcal{P} \mathbf{v}_h)|}{\|q_h\|_Q \|\mathbf{v}_h\|_V} \\ &\leq \inf_{q_h \in \text{Im} \mathcal{P}_h} \sup_{\mathbf{v}_h \in V_h} \frac{|\frac{1}{3\kappa} (q_h, \mathcal{P}_h \mathbf{v}_h)|}{\|q_h\|_Q \|\mathbf{v}_h\|_V} \end{aligned} \quad (27)$$

²⁰⁸ For a given $q_h \in \text{Im} \mathcal{P}_h$, since both q_h and $\mathcal{P}_h \mathbf{v}_h$ belong to $\text{Im} \mathcal{P}_h$, $\text{Im} \mathcal{P}_h \subset Q_h$, ²⁰⁹ according to the Cauchy-Schwarz inequality, we have:

$$\left| \frac{1}{3\kappa} (q_h, \mathcal{P}_h \mathbf{v}_h) \right| \leq \|q_h\|_Q \|\mathcal{P}_h \mathbf{v}_h\|_Q \quad (28)$$

²¹⁰ where this equality holds if and only if $q_h = \mathcal{P}_h \mathbf{v}_h$, i.e.,

$$\left| \frac{1}{3\kappa} (q_h, \mathcal{P}_h \mathbf{v}_h) \right| = \|q_h\|_Q \|\mathcal{P}_h \mathbf{v}_h\|_Q, \quad \forall \mathbf{v}_h \in V'_h \quad (29)$$

²¹¹ the space $V'_h \subseteq V_h \setminus \ker \mathcal{P}_h$ defined by:

$$V'_h = \{\mathbf{v}_h \in V_h \mid \mathcal{P}_h \mathbf{v}_h = q_h\} \quad (30)$$

²¹² And the following relationship can be evidenced:

$$\sup_{\mathbf{v}_h \in V_h} \frac{|\frac{1}{3\kappa} (q_h, \mathcal{P}_h \mathbf{v}_h)|}{\|q_h\|_Q \|\mathbf{v}_h\|_V} = \sup_{\mathbf{v}_h \in V'_h} \frac{\|\mathcal{P}_h \mathbf{v}_h\|_Q}{\|\mathbf{v}_h\|_V}, \quad \exists q_h \in \text{Im} \mathcal{P}_h \quad (31)$$

²¹³ Consequently, by combining Eqs. (27) and (31), Eq. (26) can be obtained.

²¹⁴ **Remark 1.** With Lemma 1 and the norm definitions in Eqs. (24),(25), the
²¹⁵ square of the inf-sup value can further be bounded by:

$$\beta^2 \leq \inf_{V'_h \subset V_h \setminus \ker \mathcal{P}_h} \sup_{\mathbf{v}_h \in V'_h} \frac{\|\mathcal{P}_h \mathbf{v}_h\|_Q^2}{\|\mathbf{v}_h\|_V^2} = \inf_{V'_h \subset V_h \setminus \ker \mathcal{P}_h} \sup_{\mathbf{v}_h \in V'_h} \frac{\tilde{a}(\mathbf{v}_h, \mathbf{v}_h)}{a(\mathbf{v}_h, \mathbf{v}_h)} \quad (32)$$

²¹⁶ The left-hand side of the above equation is consistent with the minimum-maximum
²¹⁷ principle [58] and again proves the equivalence with the traditional numerical
²¹⁸ inf-sup test [5]. Since that, β^2 evaluates the non-zero general eigenvalue of \tilde{a}
²¹⁹ and a in Eq. (22).

²²⁰ 3.2. Inf-sup value estimator

²²¹ Subsequently, the relationship between constraint ratio and the inf-sup con-
²²² dition is established by the following Theorem:

²²³ **Theorem 1.** Suppose that P_{n_u} is a complete polynomial space with n_u dimen-
²²⁴ sions, and V_{n_u} is the polynomial displacement space, $V_{n_u} = P_{n_u}^{n_d}$. The inf-sup
²²⁵ value β can further be bounded by:

$$\beta \leq \beta_s + O(h) \quad (33)$$

²²⁶ with

$$\beta_s = \inf_{V' \subset V_{n_u} \setminus \ker \mathcal{P}_h \mathcal{I}_h} \sup_{\mathbf{v} \in V'} \frac{\|\mathcal{P} \mathbf{v}\|_Q}{\|\mathbf{v}\|_V} \quad (34)$$

²²⁷ where \mathcal{I}_h is the interpolation operator of the displacement approximation, and
²²⁸ correspondingly, $O(h)$ is the remainder related to h .

²²⁹ PROOF. As the dimensions of V_h and V_{n_u} are identical, $\dim V_{n_u} = \dim V_h =$
²³⁰ $n_d \times n_u$. There exists a unique $\mathbf{v} \in V_{n_u}$ satisfying $\mathbf{v}_h = \mathcal{I}_h \mathbf{v}$. And the right side
²³¹ of Eq. (26) becomes:

$$\inf_{V'_h \subset V_h \setminus \ker \mathcal{P}_h} \sup_{\mathbf{v}_h \in V'_h} \frac{\|\mathcal{P}_h \mathbf{v}_h\|_Q}{\|\mathbf{v}_h\|_V} = \inf_{V' \subset V_{n_u} \setminus \ker \mathcal{P}_h \mathcal{I}_h} \sup_{\mathbf{v} \in V'} \frac{\|\mathcal{P}_h \mathcal{I}_h \mathbf{v}\|_Q}{\|\mathcal{I}_h \mathbf{v}\|_V} \quad (35)$$

²³² According to the triangular inequality, Cauchy-Schwarz inequality, and the
²³³ relationship of Eqs. (18), we have:

$$\begin{aligned} \|\mathcal{P}_h \mathcal{I}_h \mathbf{v}\|_Q &= \sup_{q_h \in Q_h} \frac{|\frac{1}{3\kappa}(q_h, \mathcal{P}_h \mathcal{I}_h \mathbf{v})|}{\|q_h\|_Q} = \sup_{q_h \in Q_h} \frac{|\frac{1}{3\kappa}(q_h, \mathcal{P} \mathcal{I}_h \mathbf{v})|}{\|q_h\|_Q} \\ &\leq \sup_{q_h \in Q_h} \frac{|\frac{1}{3\kappa}(q_h, \mathcal{P} \mathbf{v})| + |\frac{1}{3\kappa}(q_h, \mathcal{P} \mathbf{v} - \mathcal{P} \mathcal{I}_h \mathbf{v})|}{\|q_h\|_Q} \\ &\leq \|\mathcal{P} \mathbf{v}\|_Q + \|\mathcal{P}(\mathbf{v} - \mathcal{I}_h \mathbf{v})\|_Q \end{aligned} \quad (36)$$

²³⁴ Obviously, the second term on the right side of Eq. (36) is the interpolation
²³⁵ error, and can be evaluated by [59]:

$$\|\mathcal{P}(\mathbf{v} - \mathcal{I}_h \mathbf{v})\|_Q \leq Ch^k |\mathbf{v}|_{H_k} \quad (37)$$

236 where, for a sufficiently smooth $\mathbf{v} \in V$, k equals to the interpolation order of
 237 \mathcal{I}_h .

238 Further leading the relation $\|\mathcal{I}_h \mathbf{v}\|_V \geq C|\mathbf{v}|_{H_k}$ obtained from the closed
 239 graph theorem [33] and considering Eqs. (36)-(37), the right-hand side of Eq.
 240 (35) can be represented as:

$$\inf_{V' \subset V_{n_u} \setminus \ker \mathcal{P}_h \mathcal{I}_h} \sup_{\mathbf{v} \in V'} \frac{\|\mathcal{P}_h \mathcal{I}_h \mathbf{v}\|_Q}{\|\mathcal{I}_h \mathbf{v}\|_V} \leq \inf_{V' \subset V_{n_u} \setminus \ker \mathcal{P}_h \mathcal{I}_h} \sup_{\mathbf{v} \in V'} \frac{\|\mathcal{P} \mathbf{v}\|_Q}{\|\mathbf{v}\|_V} + O(h) \quad (38)$$

241 Substituting Eqs. (35),(38) into (26) finally proves Eqs. (33), (34).

242 As we can see in Eqs. (33) and (34), $\beta_s \geq 0$, the condition that β_s being
 243 equal to 0 or not determines whether the formulation can satisfy the inf-sup
 244 condition. If $\beta_s > 0$, as the mesh refines, the second term on the right-hand
 245 side of Eq. (33) will sharply reduce and can be ignored. In contrast, if $\beta_s = 0$,
 246 the second term will dominate, and the evaluation of β will be dependent to h .
 247 Therefore, the inf-sup condition is violated and numerical instability arises.

248 3.3. Polynomial-wise constraint counting

249 From the above subsection, we can know that whether β_s is zero or not
 250 determines whether the mixed-formulation can fulfill the inf-sup condition. Ac-
 251 cording to the expression of β_s in Eq. (34), as $\beta_s = 0$, the variable \mathbf{v} should
 252 belong to $\ker \mathcal{P}$, so the dimensions of the subspace in which $\beta_s \neq 0$, namely n_s ,
 253 can be evaluated by:

$$n_s = \dim(V_{n_u} \setminus \ker \mathcal{P}) \quad (39)$$

254 To further construct the relationship between the inf-sup value estimator in
 255 Eq. (33) and the constraint ratio $r = \frac{n_d \times n_u}{n_p}$, we should find the displacement
 256 and pressure DOFs in Eq. (33). With the definition of V_{n_u} , the number of
 257 displacement DOFs is easy to be evaluated by:

$$n_d \times n_u = \dim V_{n_u} \quad (40)$$

258 With well-posed nodal distributions of displacement and pressure, the number
 259 of pressure DOFs has the following relationship:

$$n_p = \dim Q_h = \dim(\text{Im} \mathcal{P}_h) = \dim(V_{n_u} \setminus \ker \mathcal{P}_h \mathcal{I}_h) \quad (41)$$

260 Figure 1 illustrates how the relationship between n_s , n_p , and n_u influences
 261 the fulfillment of the inf-sup condition:

- 262 • As $n_p > n_s$, there must exist a subspace in space $V_{n_u} \setminus \ker \mathcal{P}_h \mathcal{I}_h$ belonging
 263 to $\ker \mathcal{P}$, resulting in $\beta_s = 0$, i.e., $V_{n_u} \setminus \ker \mathcal{P}_h \mathcal{I}_h \cap \ker \mathcal{P} \neq \emptyset$. At this cir-
 264 cumstance, the inf-sup condition cannot be satisfied, and the formulation
 265 will suffer from volumetric locking.
- 266 • As $n_p \leq n_s$, for well-posed nodal distributions, the space $V_{n_u} \setminus \ker \mathcal{P}_h \mathcal{I}_h$
 267 may be a subset of $V_{n_u} \setminus \ker \mathcal{P}$. Then, β_s will remain nonzero, and the
 268 formulation will be locking-free.

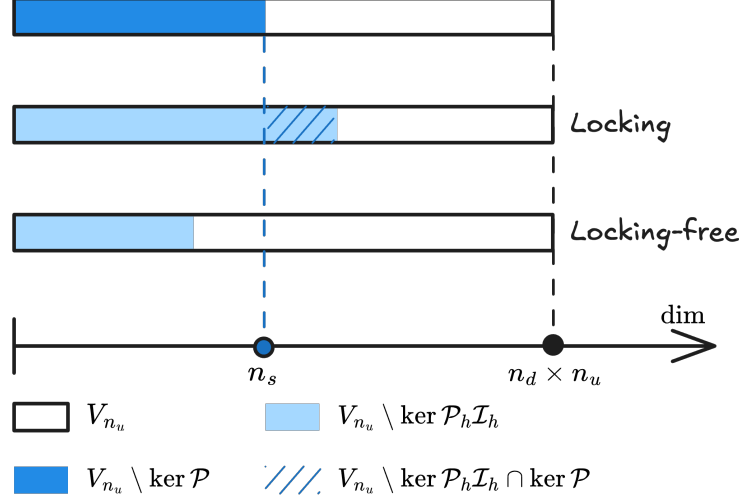


Figure 1: Illustration of estimator

269 Summarily, the formulation can satisfy the inf-sup condition and alleviate
 270 volumetric locking if at least the number of pressure nodes n_p is less than n_s ,
 271 so we name n_s as the stabilized number of pressure nodes. At this moment,
 272 the volumetric constraint ratio should meet the following relation to ensure the
 273 inf-sup condition:

$$r_{opt} \geq \frac{n_d \times n_u}{n_s} \quad (42)$$

274 **Remark 2.** *Some uniform elements with special arrangements, like the union-*
 275 *jack element arrangement for 3-node triangular elements, can pass the inf-sup*
 276 *test [6], but their pressure DOFs number is greater than n_s . This is because the*
 277 *union-jack arrangement leads to a lower nonzero eigenvalue number of \tilde{a} and a*
 278 *in Eq. (22), and the corresponding nonzero eigenvalue number is less than or*
 279 *equal to the stabilized number n_s , satisfying Eq. (42). The similar cases about*
 280 *this special element arrangement are too few, so it is more straightforward to*
 281 *use the number of pressure nodes n_p to measure $\dim(V_{n_u} \setminus \ker \mathcal{P}_h \mathcal{I}_h)$.*

282 **Remark 3.** *It is obvious that the traditional optimal constraint ratio cannot*
 283 *fulfill this condition. However, not all formulations satisfying this condition*
 284 *can totally avoid volumetric locking. This is because $n_p \leq n_s$ is not equivalent*
 285 *to $V_{n_u} \setminus \ker \mathcal{P}_h \mathcal{I}_h \subset V_{n_u} \setminus \ker \mathcal{P}$. Fortunately, well-posed nodal distributions of*
 286 *displacement and pressure can ensure this, which will be evidenced by numerical*
 287 *examples in the subsequent sections.*

288 3.4. Optimal volumetric constraint ratio

289 The fulfillment of the inf-sup condition should require the number of pres-
 290 sure nodes n_p to be lower than the stabilized number n_s , and now, we will
 291 demonstrate how to determine n_s for a specific number of displacement DOFs.

²⁹² In the 2D case, for instance, we first consider the linear polynomial displacement
²⁹³ space V_3 that is given by:

$$V_3 = \text{span} \left\{ \begin{pmatrix} 1 \\ 0 \end{pmatrix}, \begin{pmatrix} 0 \\ 1 \end{pmatrix}, \begin{pmatrix} x \\ 0 \end{pmatrix}, \begin{pmatrix} 0 \\ x \end{pmatrix}, \begin{pmatrix} y \\ 0 \end{pmatrix}, \begin{pmatrix} 0 \\ y \end{pmatrix} \right\} \quad (43)$$

²⁹⁴ or rearranged as follows,

$$V_3 = \text{span} \left\{ \underbrace{\begin{pmatrix} 1 \\ 0 \end{pmatrix}, \begin{pmatrix} 0 \\ 1 \end{pmatrix}, \begin{pmatrix} y \\ 0 \end{pmatrix}, \begin{pmatrix} 0 \\ x \end{pmatrix}, \begin{pmatrix} x \\ -y \end{pmatrix}}_{\ker \mathcal{P}}, \underbrace{\begin{pmatrix} x \\ y \end{pmatrix}}_{V_3 \setminus \ker \mathcal{P}} \right\} \quad (44)$$

²⁹⁵ It can be counted that, for $n_u = 3$, $n_s = 1$. Following the path, the displacement
²⁹⁶ space with a quadratic polynomial base, namely V_6 , can be stated as:

$$V_6 = \text{span} \left\{ \underbrace{\begin{pmatrix} 1 \\ 0 \end{pmatrix}, \begin{pmatrix} 0 \\ 1 \end{pmatrix}, \begin{pmatrix} y \\ 0 \end{pmatrix}, \begin{pmatrix} 0 \\ x \end{pmatrix}, \begin{pmatrix} x \\ -y \end{pmatrix}, \begin{pmatrix} x^2 \\ -2xy \end{pmatrix}, \begin{pmatrix} y^2 \\ 0 \end{pmatrix}, \begin{pmatrix} 0 \\ x^2 \end{pmatrix}, \begin{pmatrix} -2xy \\ y^2 \end{pmatrix}}_{\ker \mathcal{P}}, \underbrace{\begin{pmatrix} x \\ y \end{pmatrix}, \begin{pmatrix} x^2 \\ 2xy \end{pmatrix}, \begin{pmatrix} 2xy \\ y^2 \end{pmatrix}}_{V_6 \setminus \ker \mathcal{P}} \right\} \quad (45)$$

²⁹⁷ In this circumstance, $n_s = 3$. As the order of the polynomial space increases, the
²⁹⁸ optimal numbers of constraint DOFs for each order of the polynomial space are
²⁹⁹ listed in Table. 1, in which n denotes the order of space P_{n_u} . For the flexibility
³⁰⁰ of usage, the relation between n_u and n_s is summarized as follows:

$$n_s = \frac{n(n+1)}{2}, \quad n = \left\lfloor \frac{\sqrt{1+8n_u}-3}{2} \right\rfloor \quad (46)$$

³⁰¹ where $\lfloor \bullet \rfloor$ denotes the floor function.

Table 1: Relationship between the number of displacement nodes n_u and stabilized number of pressure nodes n_s

n	2D		3D	
	n_u	n_s	n_u	n_s
1	3	1	4	1
2	6	3	10	4
3	10	6	20	10
4	15	10	35	20
\vdots	\vdots	\vdots	\vdots	\vdots

³⁰² For the 3D case, following the path in 2D, the linear polynomial space V_4 is

³⁰³ considered herein, and the arranged space of V_4 is listed as follows:

$$V_4 = \text{span} \left\{ \underbrace{\begin{pmatrix} 1 \\ 0 \\ 0 \\ 0 \end{pmatrix}, \begin{pmatrix} 0 \\ 1 \\ 0 \\ 0 \end{pmatrix}, \begin{pmatrix} 0 \\ 0 \\ 1 \\ 0 \end{pmatrix}, \begin{pmatrix} 0 \\ x \\ 0 \\ 0 \end{pmatrix}, \begin{pmatrix} 0 \\ 0 \\ x \\ 0 \end{pmatrix}, \begin{pmatrix} 0 \\ 0 \\ 0 \\ y \end{pmatrix}}_{\ker \mathcal{P}}, \underbrace{\begin{pmatrix} 0 \\ 0 \\ y \\ 0 \end{pmatrix}, \begin{pmatrix} z \\ 0 \\ 0 \\ 0 \end{pmatrix}, \begin{pmatrix} 0 \\ z \\ 0 \\ 0 \end{pmatrix}, \begin{pmatrix} x \\ -y \\ 0 \\ 0 \end{pmatrix}, \begin{pmatrix} x \\ 0 \\ -z \\ 0 \end{pmatrix}, \begin{pmatrix} x \\ y \\ z \\ 0 \end{pmatrix}}_{\ker \mathcal{P}} \right\}_{V_{n_u} \setminus \ker \mathcal{P}} \quad (47)$$

³⁰⁴ For brevity, the stabilized numbers for higher-order polynomial displacement
³⁰⁵ spaces are directly listed in Table. 1, and it can be summarized that, for a given
³⁰⁶ number of displacement DOFs, the stabilized number for pressure DOFs can be
³⁰⁷ calculated as follows:

$$n_s = \frac{n(n+1)(n+2)}{6} \quad (48)$$

$$n = \left\lfloor \left(3n_u + \frac{1}{3} \sqrt{81n_u^2 - \frac{1}{3}} \right)^{\frac{1}{3}} + \frac{1}{3 \left(3n_u + \frac{1}{3} \sqrt{81n_u^2 - \frac{1}{3}} \right)^{\frac{1}{3}}} - 2 \right\rfloor \quad (49)$$

³⁰⁸ 4. Mixed FE–meshfree formulation with optimal constraint ratio

³⁰⁹ In the proposed mixed–formulation, the displacement is approximated using
³¹⁰ 3-node (Tri3), 6-node (Tri6) triangular elements and 4-node (Quad4), 8-node
³¹¹ (Quad8) quadrilateral elements in 2D, 4-node (Tet4) tetrahedral element and
³¹² 8-node (Hex8) hexahedral element in 3D [2]. In order to flexibly adjust to let
³¹³ the DOFs of pressure meet the optimal constraint, the reproducing kernel (RK)
³¹⁴ meshfree approximation is involved to approximate pressure, namely “FE”–RK
³¹⁵ formulation.

³¹⁶ 4.1. Reproducing kernel meshfree approximation

³¹⁷ In accordance with the reproducing kernel approximation, the entire domain
³¹⁸ Ω , as shown in Figure 2, is discretized by n_p meshfree nodes, $\{\mathbf{x}_I\}_{I=1}^{n_p}$. The
³¹⁹ approximated pressure, namely p_h , can be expressed by the shape function Ψ_I
³²⁰ and nodal coefficient p_I , yields:

$$p_h(\mathbf{x}) = \sum_{I=1}^{n_p} \Psi_I(\mathbf{x}) p_I \quad (50)$$

³²¹ where, in the reproducing kernel approximation framework, the shape function
³²² Ψ_I is given by:

$$\Psi_I(\mathbf{x}) = \mathbf{c}(\mathbf{x}_I - \mathbf{x}) \mathbf{p}(\mathbf{x}_I - \mathbf{x}) \phi(\mathbf{x}_I - \mathbf{x}) \quad (51)$$

³²³ in which \mathbf{p} is the basis vector, for instance in the context of the 3D quadratic
³²⁴ case, the basis vector takes the following form:

$$\mathbf{p}(\mathbf{x}) = \{1, x, y, z, x^2, y^2, z^2, xy, xz, yz\}^T \quad (52)$$

³²⁵ and ϕ stands for the kernel function. In this work, the traditional Cubic B-spline
³²⁶ function with square or cube support is used as the kernel function:

$$\phi(\mathbf{x}_I - \mathbf{x}) = \phi(s_x)\phi(s_y)\phi(s_z), \quad s_i = \frac{\|\mathbf{x}_I - \mathbf{x}\|}{\bar{s}_{iI}} \quad (53)$$

³²⁷ with

$$\phi(s) = \frac{1}{3!} \begin{cases} (2-2s)^3 - 4(1-2s)^3 & s \leq \frac{1}{2} \\ (2-2s)^3 & \frac{1}{2} < s < 1 \\ 0 & s > 1 \end{cases} \quad (54)$$

³²⁸ where \bar{s}_{iI} 's are the support size towards the i -direction for the shape function
³²⁹ Ψ_I . The correction function \mathbf{c} can be determined by the following so-called
³³⁰ consistency condition:

$$\sum_{I=1}^{n_p} \Psi_I(\mathbf{x}) \mathbf{p}(\mathbf{x}_I) = \mathbf{p}(\mathbf{x}) \quad (55)$$

³³¹ or equivalent shifted form:

$$\sum_{I=1}^{n_p} \Psi_I(\mathbf{x}) \mathbf{p}(\mathbf{x}_I - \mathbf{x}) = \mathbf{p}(\mathbf{0}) \quad (56)$$

³³² The consistency condition ensures that the reproducing kernel shape functions
³³³ are able to reproduce the polynomial space spanned by the basis function \mathbf{p} ,
³³⁴ which is a fundamental requirement for the accuracy of the Galerkin method.
³³⁵ Herein, the order of the basis function \mathbf{p} is chosen to be the same as the order
³³⁶ of the displacement approximation.

³³⁷ Further, substituting Eq. 51 into Eq. (56) leads to:

$$\mathbf{c}(\mathbf{x}_I - \mathbf{x}) = \mathbf{A}^{-1}(\mathbf{x}_I - \mathbf{x}) \mathbf{p}(\mathbf{0}) \quad (57)$$

³³⁸ in which \mathbf{A} is namely the moment matrix evaluated by:

$$\mathbf{A}(\mathbf{x}_I - \mathbf{x}) = \sum_{I=1}^{n_p} \mathbf{p}(\mathbf{x}_I - \mathbf{x}) \mathbf{p}^T(\mathbf{x}_I - \mathbf{x}) \phi(\mathbf{x}_I - \mathbf{x}) \quad (58)$$

³³⁹ Taking Eq. (57) back to Eq. (51), the final form of the reproducing kernel shape
³⁴⁰ function can be obtained as:

$$\Psi_I(\mathbf{x}) = \mathbf{p}^T(\mathbf{0}) \mathbf{A}^{-1}(\mathbf{x}_I - \mathbf{x}) \phi(\mathbf{x}_I - \mathbf{x}) \quad (59)$$

³⁴¹ As shown in Figure 2, reproducing kernel meshfree shape functions are glob-
³⁴² ally smooth across the entire domain, using them to discretize the pressure field

343 allows the constraint ratio to be adjusted arbitrarily, without being limited by
 344 element topology. Meshfree shape functions generally lack the Kronecker delta
 345 property, which prevents the direct imposition of essential boundary conditions.
 346 Fortunately, the mixed formulation shown in Eq. 14 only concerns the displace-
 347 ment essential boundary condition, and this condition can be easily imposed by
 348 the standard methods, such as the penalty method that used in this work.

349 Moreover, when combined with finite element approximations in Eq. 14,
 350 numerical integration can be conveniently performed within each finite element
 351 (Ω_C 's). The numerical integration issue caused by the loss of variational con-
 352 sistency between meshfree shape functions and their derivatives [60] would not
 353 appear in the mixed formulation of Eq. 14, this is due to the fact that Eq.
 354 14 solely depends on the meshfree shape functions themselves. Therefore, the
 355 proposed method employs standard lower-order Gaussian quadrature rules, as
 356 commonly used in traditional finite element methods, while still maintaining its
 357 accuracy. Table 2 lists the integration schemes used in this work for mixed-
 358 formulations. Methods with linear basis functions use an integration scheme of
 359 order 2. Those with quadratic basis functions use a scheme of order 4. The
 360 detailed locations and weights of the Gauss points can be found in Ref. [4].

Table 2: Integration schemes for the mixed FE–meshfree formulation

Methods	n_o	n_g for Ω	n_g for Γ
Tri3-RK	2	3	2
Tri6-RK	4	6	3
Quad4-RK	2	2×2	2
Quad8-RK	4	3×3	3
Tet4-RK	2	4	3
Hex8-RK	2	$2 \times 2 \times 2$	4

n_o : Integration Order n_g : Number of integration points

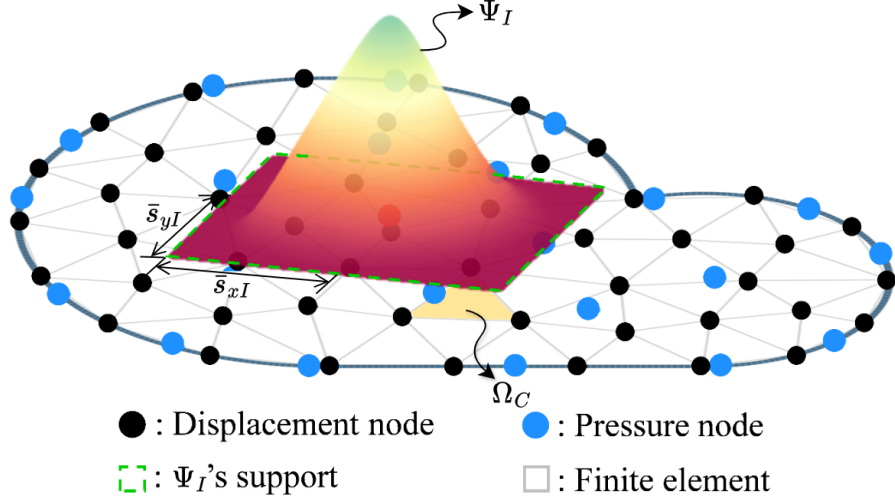


Figure 2: Illustration for reproducing kernel meshfree approximation

361 *4.2. Pressure node distributions with optimal constraint ratio*

362 In this subsection, 2D and 3D inf-sup tests [6], as defined in Eq. 32, are
363 conducted using the mixed FE-meshfree formulations to validate the proposed
364 inf-sup value estimator. The 2D test considers the square domain $\Omega = (0, 1) \times$
365 $(0, 1)$, where the displacement is discretized by Tri3 and Quad4 with 4×4 ,
366 8×8 , 16×16 and 32×32 elements, Tri6 and Quad8 with 2×2 , 4×4 , 8×8
367 and 16×16 elements, respectively. The 3D test employs a cube domain $\Omega =$
368 $(0, 1) \times (0, 1) \times (0, 1)$ with 4×4 , 8×8 and 16×16 elements for the Tet4 and Hex8.
369 For pressure discretization, linear meshfree approximation with a normalized
370 support size of 1.5 is employed for Tri3, Quad4, Tet4 and Hex8. For Tri6 and
371 Quad8, a quadratic meshfree approximation with a normalized support size of
372 2.5 is utilized. In order to avoid the influence of interpolation error, uniform
373 nodal distributions are used for pressure discretizations, for example in Figure
374 3, which displays 4×4 Quad4 elements with 4×3 uniformly distributed pressure
375 nodes.

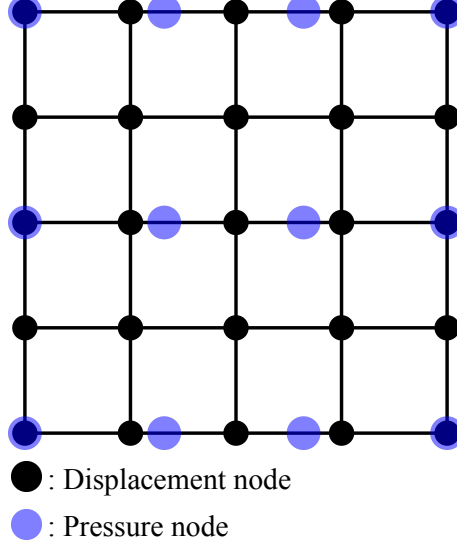


Figure 3: Illustration of uniform nodal distribution for inf-sup test with $n_u = 5 \times 5$, $n_p = 4 \times 3$

Figures 4–9 show the corresponding results, in which the red line stands for the value of β with respect to the number of pressure nodes n_p , and the vertical dashed line denotes the stabilized number n_s . The deeper color of the lines means mesh refinement. The results show that, no matter linear or quadratic elements, as n_p increases over n_s , the value of β sharply decreases, and then the inf-sup condition cannot be maintained. This result is consistent with the discussion in Section 3, and again verifies the effect of the proposed estimator.

Moreover, the mixed formulation's results with the traditional optimal constraint ratio $r = n_d$ are listed in these figures as well, and β in this circumstance is already much smaller than those in the optimal range. Considering the results shown above, the easy programming and efficiency, the pressure nodes are chosen among the displacement nodes. The optimal schemes for linear and quadratic, 2D and 3D element discretizations, namely with $r = r_{opt}$, are shown in Figure 10, where every other displacement node is selected as the pressure node. For practical implementations of linear cases, the pressure nodes are initially generated using traditional approaches, such as Delaunay triangulation. Subsequently, the displacement nodes are then obtained through a standard mesh refinement process to the pressure nodes. For quadratic approximations in Tri6 and Quad8 elements, the element vertices are chosen as pressure nodes after displacement element generation. Consequently, all constraint ratios evaluated using the discretizations in Figure 10 fall within the optimal range. The corresponding inf-sup test results for these schemes are also marked in inf-sup test figure and show that, with mesh refinement, their β 's are always maintained at a non-negligible level.

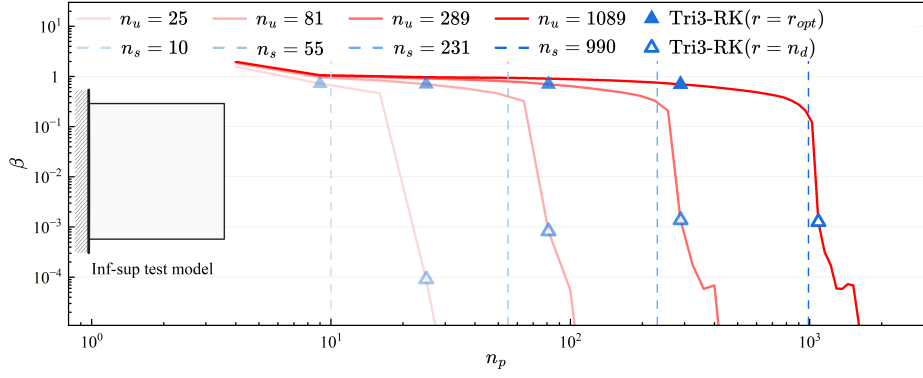


Figure 4: Inf-sup test for Tri3-RK

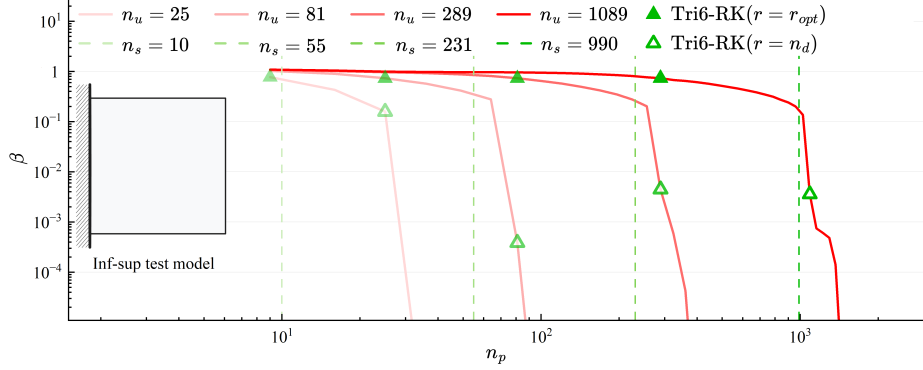


Figure 5: Inf-sup test for Tri6-RK

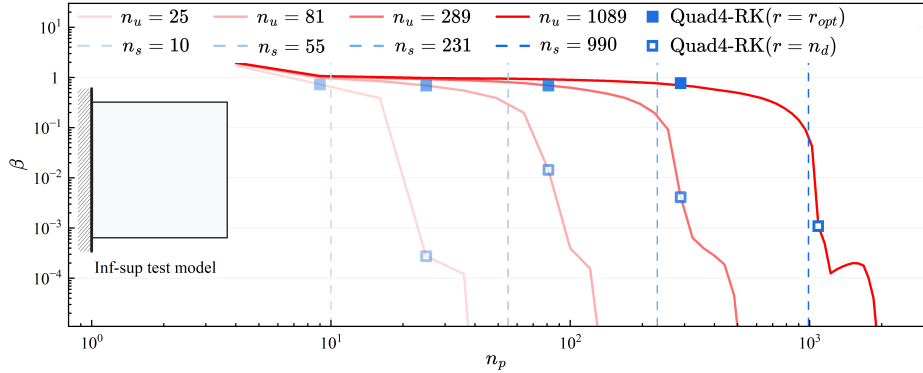


Figure 6: Inf-sup test for Quad4-RK

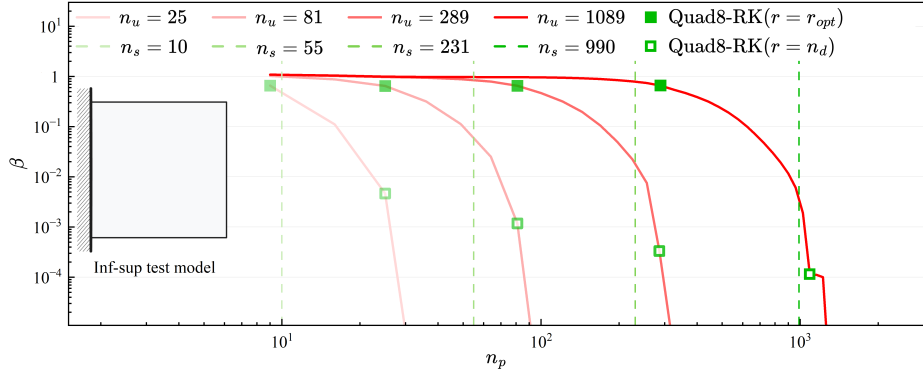


Figure 7: Inf-sup test for Quad8-RK

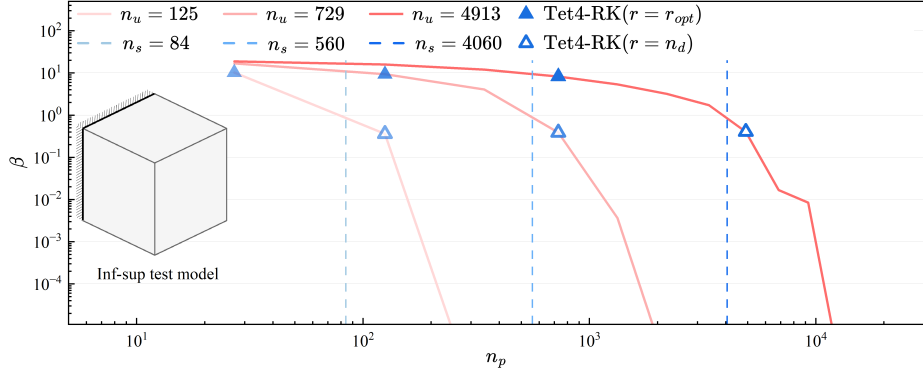


Figure 8: Inf-sup test for Tet4-RK

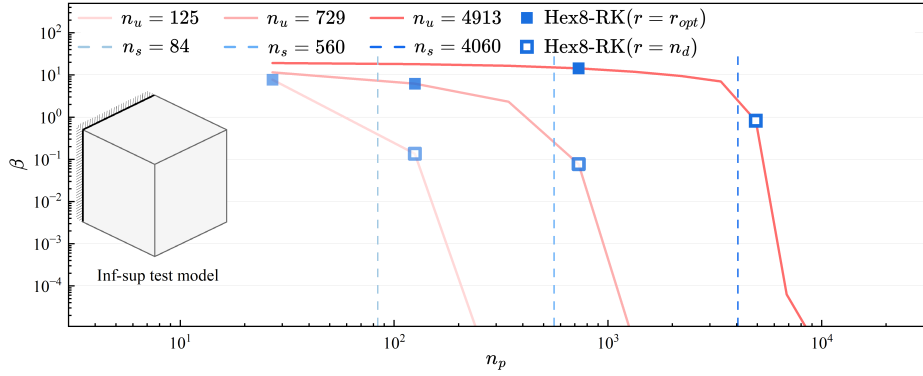


Figure 9: Inf-sup test for Hex8-RK

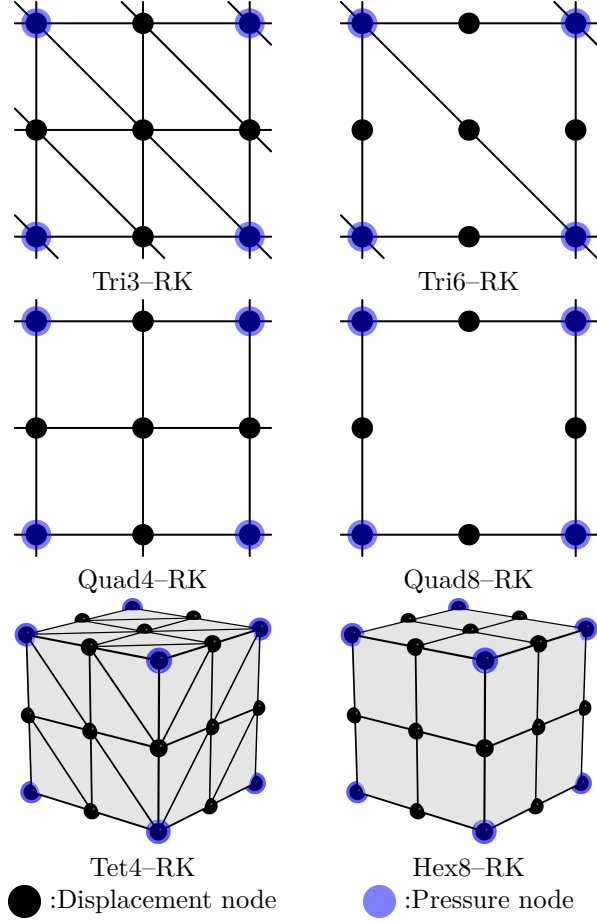


Figure 10: Nodal distribution schemes for mixed FE-meshfree formulations with $r = r_{opt}$

400 5. Numerical examples

401 5.1. Cantilever beam problem

402 Consider the cantilever beam problem shown in Figure 11 with length $L =$
403 $D = 12$, and the incompressible material parameters are employed
404 with Young's modulus $E = 3 \times 10^6$, Poisson's ratio $\nu = 0.5 - 10^{-8}$. The left hand
405 side is fixed and the right side subject to a concentrated force $P = 1000$. All
406 the prescribed values in the boundary conditions are evaluated by the analytical
407 solution that is given as follows [61]:

$$\begin{cases} u_x(\mathbf{x}) = -\frac{Py}{6EI} \left((6L - 3x)x + (2 + \bar{\nu})(y^2 - \frac{D^2}{4}) \right) \\ u_y(\mathbf{x}) = \frac{P}{6EI} \left(3\bar{\nu}y^2(L - x) + (4 + 5\bar{\nu})\frac{D^2x}{4} + (3L - x)x^2 \right) \end{cases} \quad (60)$$

408 where I is the beam's moment of inertia, \bar{E} and $\bar{\nu}$ are the material parameters
 409 for plane strain hypothesis, they can be expressed by:

$$I = \frac{D^3}{12}, \quad \bar{E} = \frac{E}{1 - \nu^2}, \quad \bar{\nu} = \frac{\nu}{1 - \nu} \quad (61)$$

410 And correspondingly, the stress components and the pressure are evaluated by

$$\begin{cases} \sigma_{xx} = -\frac{P(L-x)y}{I} \\ \sigma_{yy} = 0 \\ \sigma_{xy} = \frac{P}{2I}\left(\frac{D^2}{4} - y^2\right) \\ p = -\frac{P(1+\nu)(L-x)y}{3I} \end{cases} \quad (62)$$

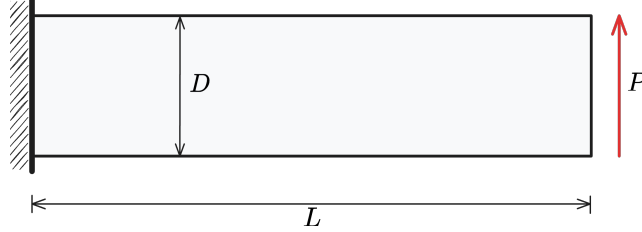


Figure 11: Illustration of cantilever beam problem

411 In this problem, the Tri3, Quad4 elements with 16×4 , 32×8 , 64×16 , 128×32
 412 grids, and Tri6, Quad8 elements with 8×2 , 16×4 , 32×8 , 64×16 grids are
 413 employed for displacement discretization. The pressure is discretized by linear
 414 and quadratic meshfree approximations with 1.5 and 2.5 characterized support
 415 sizes respectively. The strain and pressure errors with respect to pressure nodes
 416 n_p are displayed in Figures 12, 13, where, to avoid the interpolation error, the
 417 pressure nodes are uniformly distributed independent with displacement nodes
 418 by the same way in Section 4.2. The vertical dashed lines stand for the stabilized
 419 number n_s . The figures imply that all pressure errors immediately increase when
 420 their constraint ratios are out of the optimal range, and quadratic elements still
 421 have better results than linear elements. As n_p becomes very small, the pressure
 422 errors do not increase. This is because the pressure error estimator in Eq. (A.14)
 423 is primarily controlled by the strain error and the inf-sup value β . The exact
 424 pressure solution in Eq. (62) is only a second-order polynomial. As a result, the
 425 pressure interpolation error in Eq. (A.14) is either very small or nonexistent.
 426 For the strain error, the Quad8-RK method shows stable results regardless of
 427 whether the constraint ratio is in the optimal range. This may be due to the
 428 fact that the Quad8 element with a regular mesh satisfies the relationship of
 429 Eq. (A.16). In this context, the strain error of Eq. (A.10) is independent of the
 430 inf-sup value β and remains at a low level.

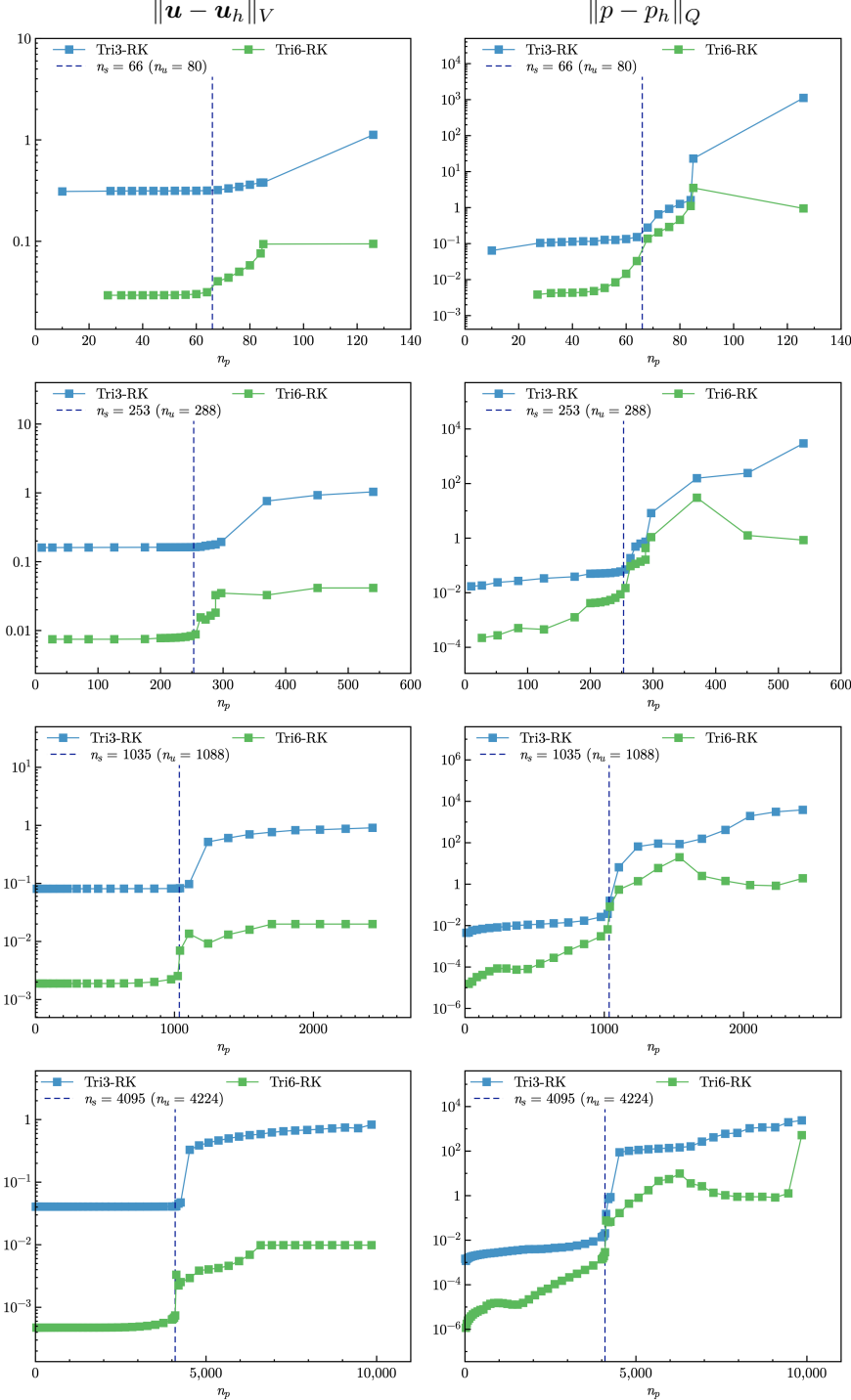


Figure 12: Strain and pressure errors vs. n_p for cantilever beam problem with triangular elements

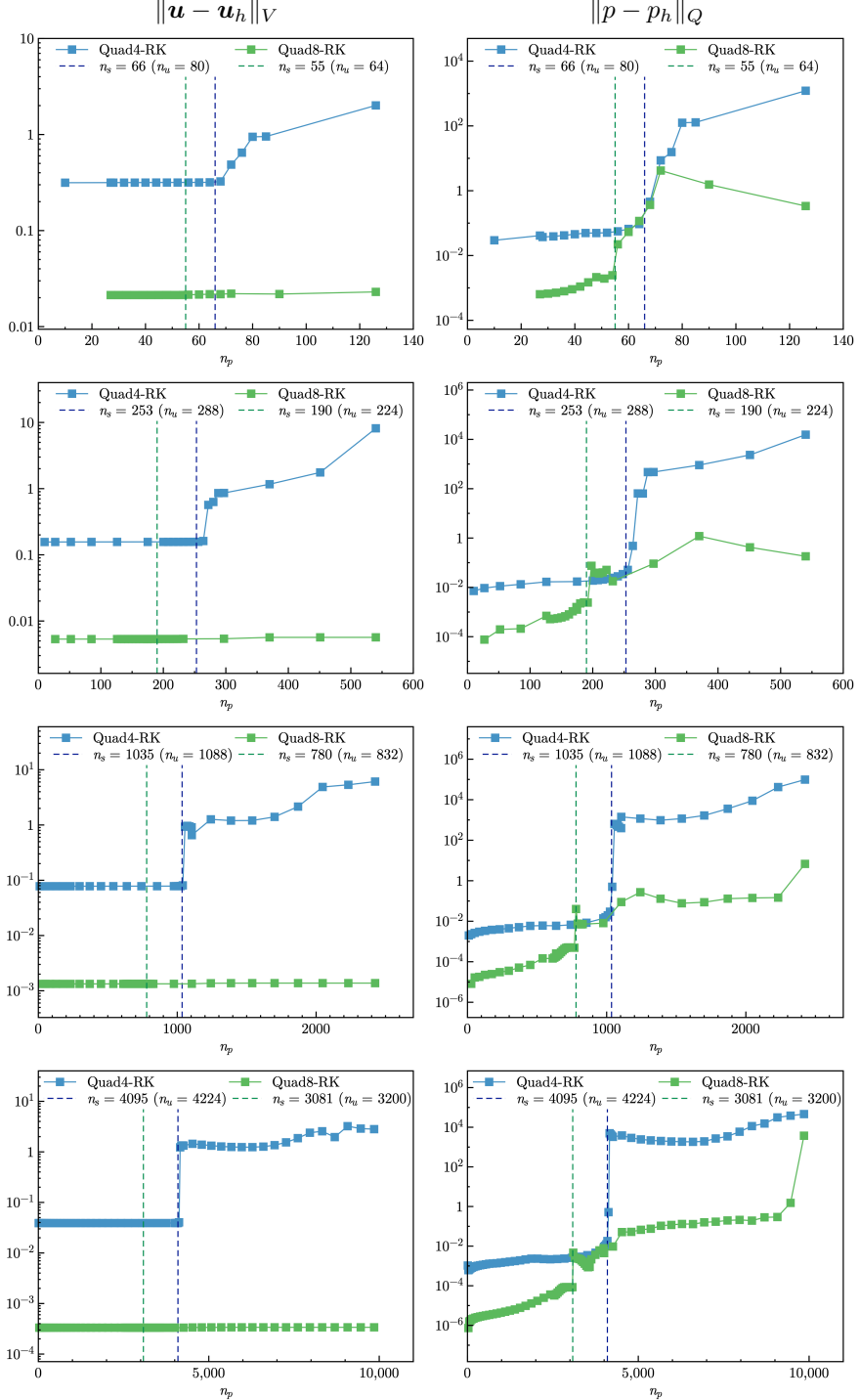


Figure 13: Strain and pressure errors vs. n_p for cantilever beam problem with quadrilateral elements

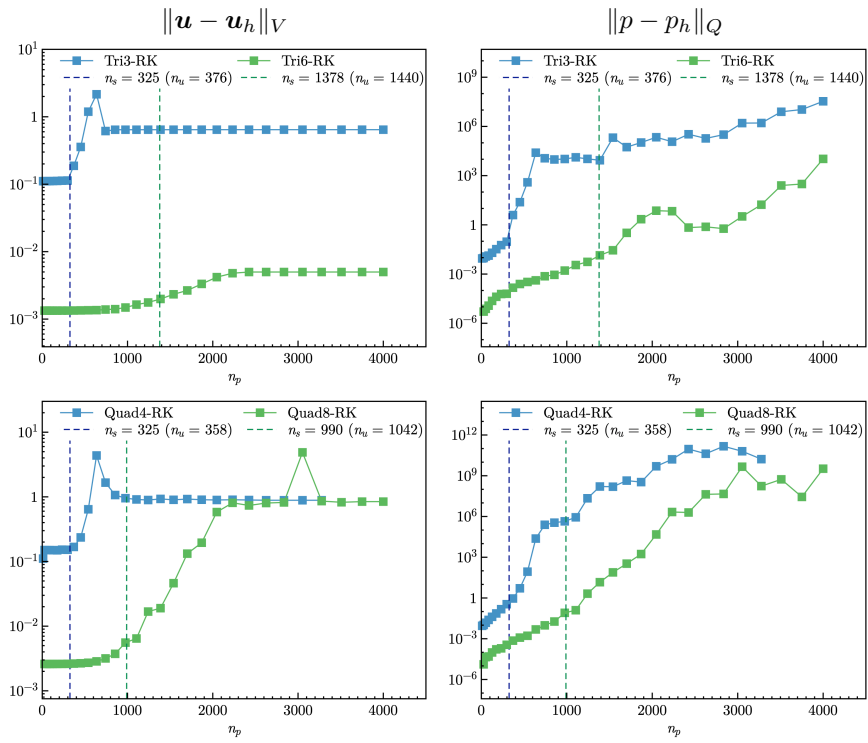


Figure 14: Strain and pressure errors vs. n_p for cantilever beam problem with non-uniform elements

Figures 15, 16 are the strain and pressure error convergence studies for triangular and quadrilateral elements, respectively, in which Tri3–RK, Tri6–RK with $r = n_d$, the MINI element [32], 6–node triangular displacement element with 3–node continuous triangular pressure element (T6C3) are the comparative methods for Tri3–RK and Tri6–RK with $r = r_{opt}$, and Quad4–RK, Quad8–RK with $r = n_d$, 4–node quadrilateral displacement element with 1–node piecewise constant pressure (Q4P1), 8–node quadrilateral displacement element with 3–node piecewise linear pressure (Q8P3) are employed for comparison with Quad4–RK and Quad8–RK with $r = r_{opt}$. Except Tri3–RK, Quad8–RK with $r = n_d$ for strain error, all formulations with the traditional constraint ratio of $r = n_d$ cannot ensure the optimal error convergence rates. The proposed mixed formulations with $r = r_{opt}$ can maintain the optimal error convergence ratio, except the strain error of Quad8–RK is a little larger than that of Q8P3, the proposed approaches show the best performance in accuracy.

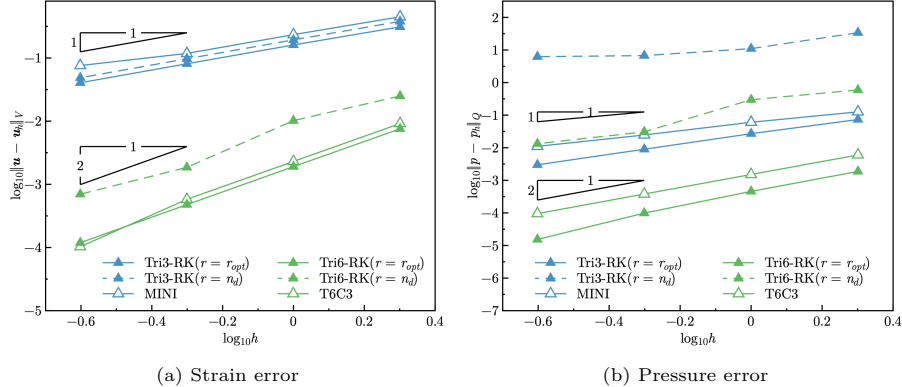


Figure 15: Error convergence study for cantilever beam problem with triangular elements

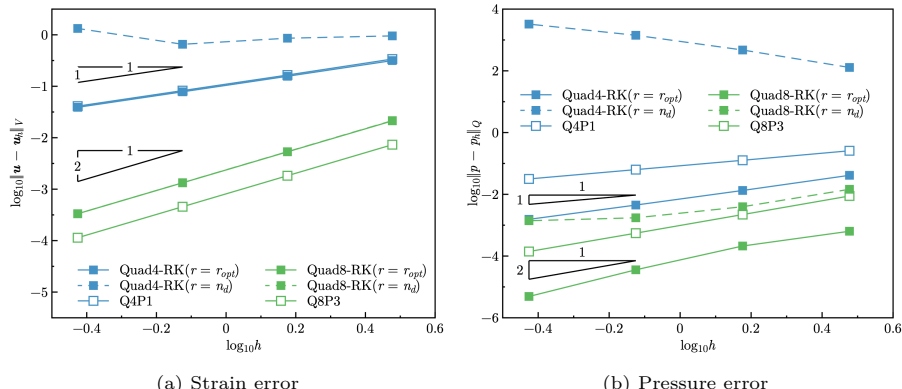


Figure 16: Error convergence study for cantilever beam problem with quadrilateral elements

445 5.2. Plate with hole problem

446 Consider an infinite plate with a hole centered at the origin, as shown in
 447 Figure 17, and at the infinity towards the x -direction subjected to a uniform
 448 traction $T = 1000$. The geometric and material parameters for this problem are
 449 that the ratio of the hole $a = 1$, Young's modulus $E = 3 \times 10^6$, and Poisson's
 450 ratio $\nu = 0.5 - 10^{-8}$. The analytical solution of this problem refers to the
 451 Michell solution [61] as:

$$\begin{cases} u_x(\rho, \theta) = \frac{T a}{8\mu} \left(\frac{\rho}{a} (k+1) \cos \theta - \frac{2a^3}{\rho^3} \cos 3\theta + \frac{2a}{\rho} ((1+k) \cos \theta + \cos 3\theta) \right) \\ u_y(\rho, \theta) = \frac{T a}{8\mu} \left(\frac{\rho}{a} (k-3) \sin \theta - \frac{2a^3}{\rho^3} \sin 3\theta + \frac{2a}{\rho} ((1-k) \sin \theta + \sin 3\theta) \right) \end{cases} \quad (63)$$

452 in which $k = \frac{3-\nu}{1+\nu}$, $\mu = \frac{E}{2(1+\nu)}$. And the stress components are given by:

$$\begin{cases} \sigma_{xx} = T \left(1 - \frac{a^2}{\rho^2} \left(\frac{3}{2} \cos 2\theta + \cos 4\theta \right) + \frac{3a^4}{2\rho^4} \cos 4\theta \right) \\ \sigma_{yy} = -T \left(\frac{a^2}{\rho^2} \left(\frac{1}{2} \cos 2\theta - \cos 4\theta \right) + \frac{3a^4}{2\rho^4} \cos 4\theta \right) \\ \sigma_{xy} = -T \left(\frac{a^2}{\rho^2} \left(\frac{1}{2} \sin 2\theta + \sin 4\theta \right) - \frac{3a^4}{2\rho^4} \sin 4\theta \right) \end{cases} \quad (64)$$

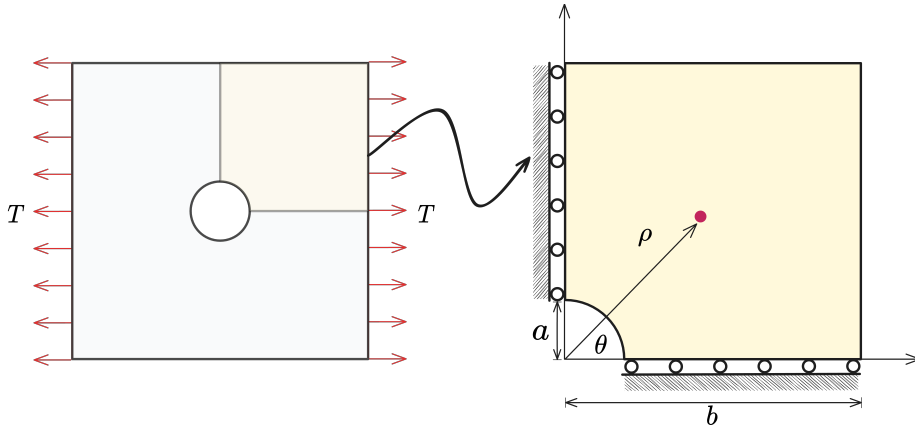


Figure 17: Illustration of plate with hole problem

453 According to the symmetry property of this problem, only a quarter model
 454 with length $b = 5$ is considered as shown in Figure 17. The displacement is
 455 discretized by 3-node, 6-node triangular elements, 4-node and 8-node quadrilater-
 456 al elements. The corresponding linear and quadratic meshfree formulations
 457 are employed for pressure discretization, and the characterized support sizes
 458 are chosen as 1.5 and 2.5, respectively. Figures 18, 19 study the relationship

459 between strain, pressure errors, and n_p using the nodal distributions uniformly
460 related to displacement nodes. Unlike the quadrilateral element case in Section
461 5.1, both displacement and pressure errors in this problem increase as n_p reduces
462 to a small value. Tri3–RK exhibits less sensitivity in strain error than Tri6–RK.
463 This may be because, as shown in Eqs. (A.10) and (A.20), the displacement
464 approximation error for the space of $\ker \mathcal{P}_h$ does not increase as immediately
465 when $\frac{C_p}{\beta}$ in Eq. (A.20) is not too much larger than 1. However, its error in-
466 creases as n_p goes up. Both FE–RK with constraint ratios under the optimal
467 range perform acceptably.

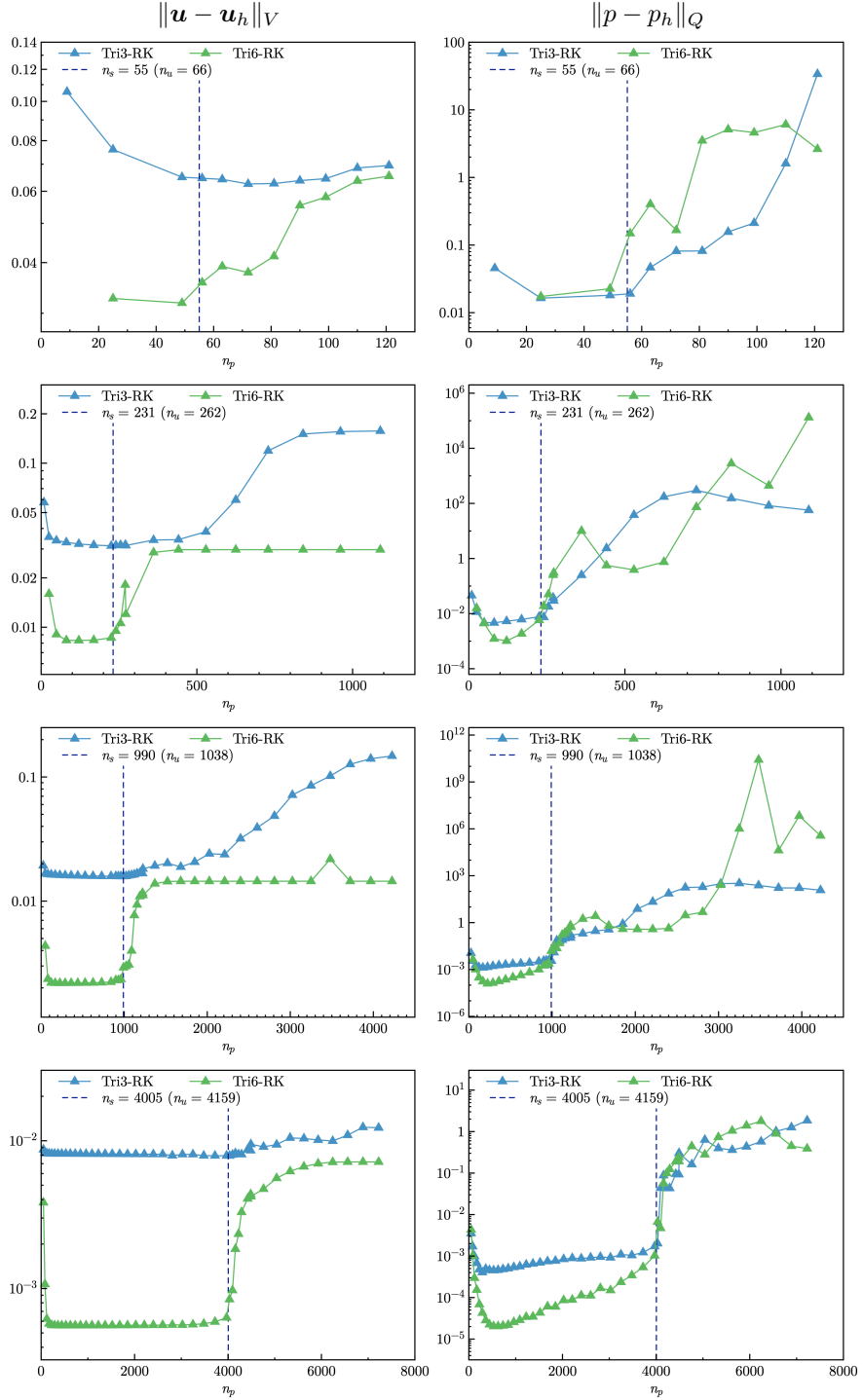


Figure 18: Strain and pressure errors vs. n_p for plate with hole problem

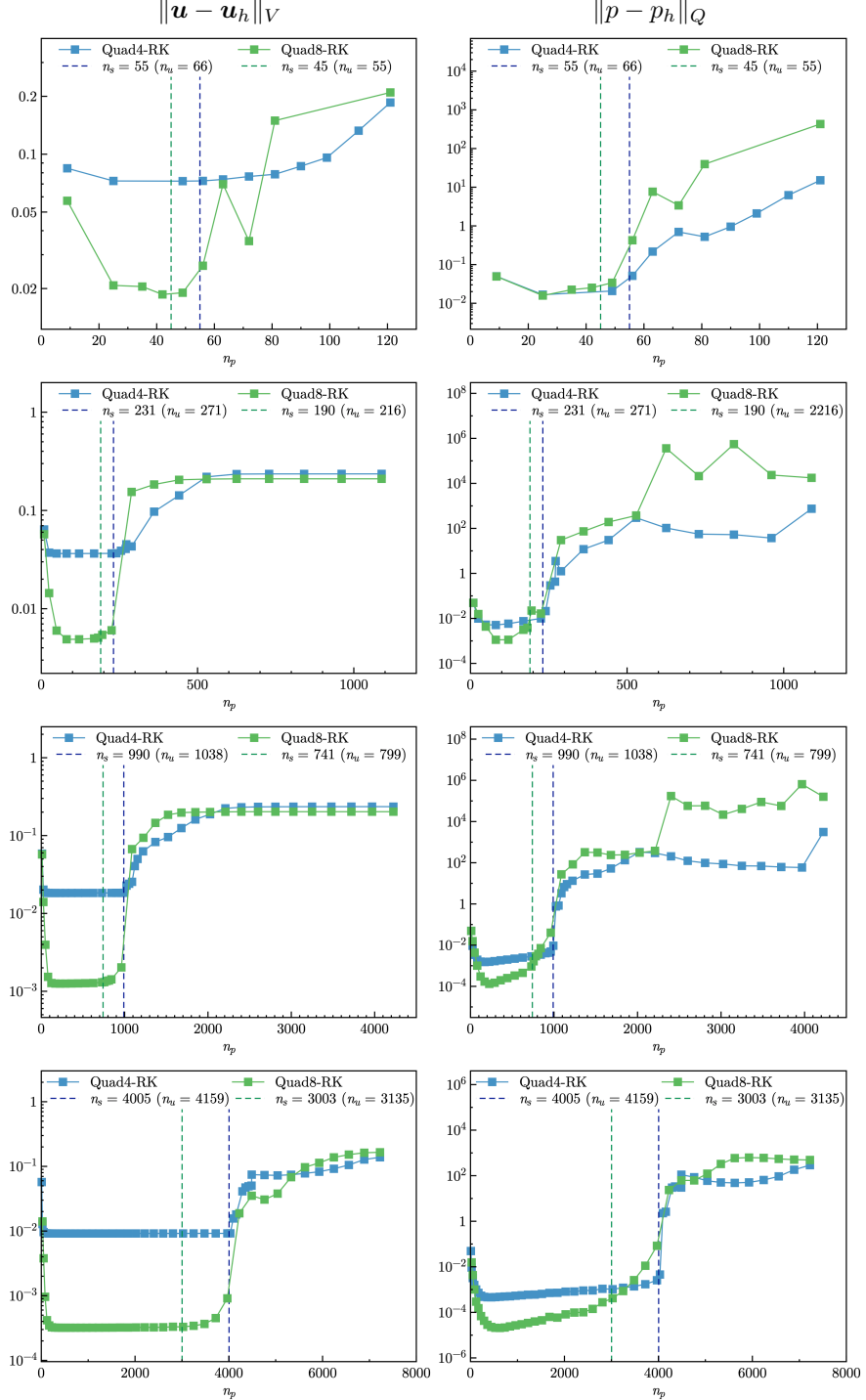


Figure 19: Strain and pressure errors vs. n_p for plate with hole problem

468 The corresponding error convergence studies are presented in Figures 20, 21,
 469 the results show that only Tri3–RK with $r = 2$ shows a comparable result with
 470 the optimal one with $r = r_{opt}$ in strain error. The other formulations with the
 471 traditional constraint ratio show lower accuracy and error convergence rates.

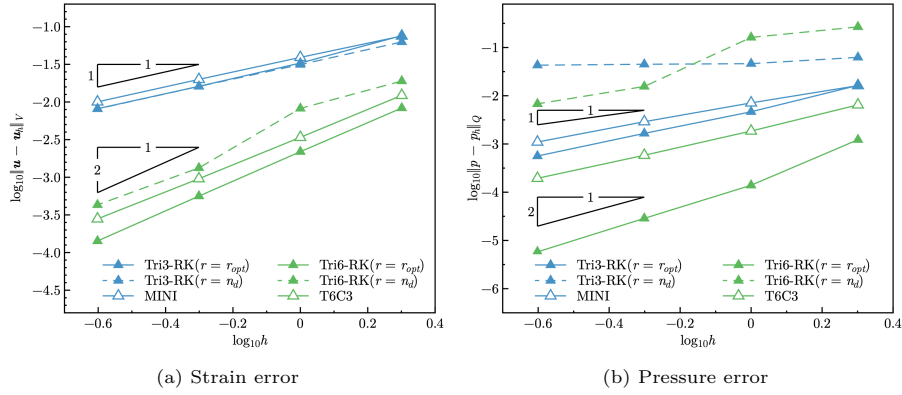


Figure 20: Error convergence study for plate with a hole problem with triangular elements

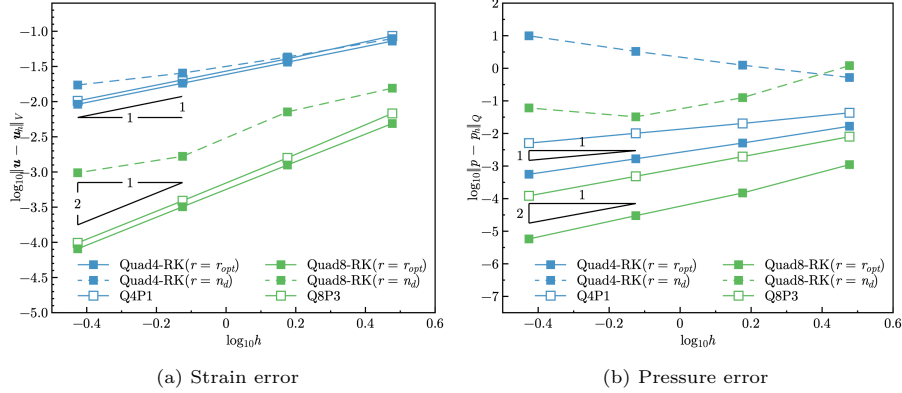


Figure 21: Error convergence study for plate with a hole problem with quadrilateral elements

472 Furthermore, the influence of the integration scheme for this problem is
 473 investigated. As shown in Tables 3 and 4, the integration order n_o is varied
 474 from 1 to 5 for triangular elements and from 1 to 11 for quadrilateral elements.
 475 The results show that the proposed mixed formulations are not sensitive to the
 476 integration order. Using the traditional lower-order Gauss integration scheme
 477 can sufficiently obtain accurate results. This is consistent with the previous
 478 analysis in Section 4.1.

Table 3: Error comparison with different triangular integration schemes for plate with a hole problem

n_o	n_g for Ω	n_g for Γ	Tri3-RK		Tri6-RK	
			$\ \mathbf{u} - \mathbf{u}_h\ _V$	$\ p - p_h\ _Q$	$\ \mathbf{u} - \mathbf{u}_h\ _V$	$\ p - p_h\ _Q$
1	1	1	3.11E-2	3.53E-3	8.53E17	1.31E4
2	3	2	3.11E-2	3.67E-3	8.33E-3	1.20E-3
3	4	2	3.11E-2	3.67E-3	8.32E-3	1.20E-3
4	6	3	3.11E-2	3.68E-3	8.32E-3	1.22E-3
5	7	3	3.11E-2	3.68E-3	8.32E-3	1.22E-3

n_o : Integration order n_g : Number of integration points

Table 4: Error comparison with different quadrilateral integration schemes for plate with a hole problem

n_o	n_g for Ω	n_g for Γ	Quad4-RK		Quad8-RK	
			$\ \mathbf{u} - \mathbf{u}_h\ _V$	$\ p - p_h\ _Q$	$\ \mathbf{u} - \mathbf{u}_h\ _V$	$\ p - p_h\ _Q$
1	3	1	3.64E-2	5.01E-3	9.53E13	8.15E-1
3	2×2	2	3.64E-2	5.09E-3	4.33E-2	8.84E-3
5	3×3	3	3.62E-2	3.71E-3	1.27E-3	4.42E-5
7	4×4	4	3.62E-2	3.70E-3	1.26E-3	1.49E-4
9	5×5	5	3.62E-2	3.70E-3	1.26E-3	1.50E-4
11	6×6	6	3.62E-2	3.70E-3	1.26E-3	1.50E-4

n_o : Integration Order n_g : Number of integration points

5.3. Cook's membrane problem

The Cook's membrane problem [12] is used herein for stability analysis of pressure. The geometry of this problem is shown in Figure 22, in which the left hand side is fixed and the right hand side subjects a concentrated force $P = 6.25$ in the y -direction. The material parameters are Young's modulus $E = 70.0$ and Poisson's ratio $\nu = 0.5 - 10^{-8}$.

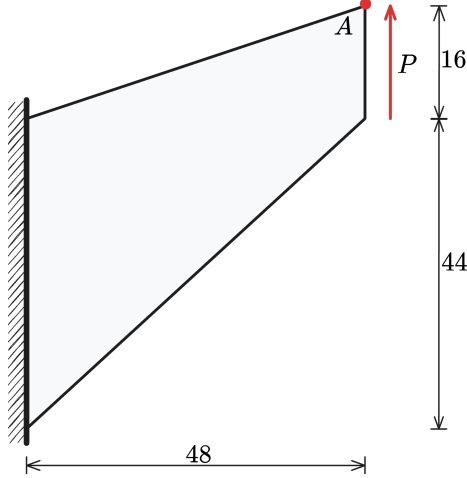


Figure 22: Illustration of Cook's membrane problem

In this test, we evaluated the convergence properties by comparing the vertical displacement at point A against a reference value of 28.0. As shown in Figure 23 illustrates, the methods employing $r = r_{opt}$ produced results that were notably closer to this reference value than those using $r = n_d$. Furthermore, to investigate stability, Figures 24–27 show the pressure contour plots for non-uniform Tri3–RK, Tri6–RK, Quad4–RK, and Quad8–RK formulations with $r = n_d$ and $r = r_{opt}$, respectively. The reproducing kernel meshfree approximations are employed for pressure discretization with characterized support sizes of 1.5 for the linear basis function and 2.5 for the quadratic basis function. The results imply that the pressure contour plots with the optimal constraint ratio $r = r_{opt}$ show a more stable and smooth pressure distribution compared to those with the traditional constraint ratio $r = n_d$.

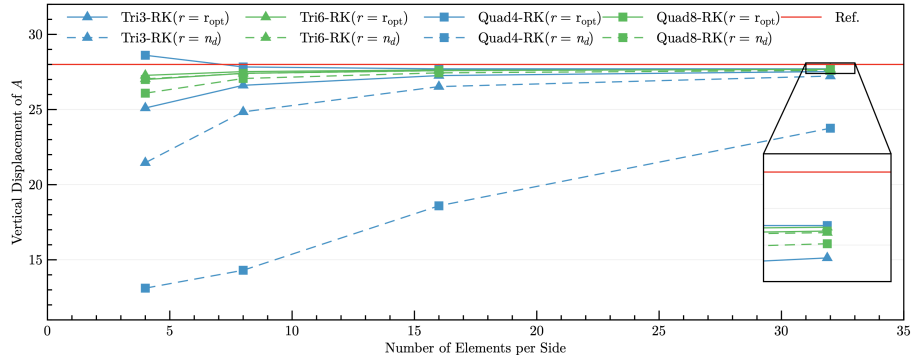


Figure 23: Convergence comparison of the vertical displacement at point A for Cook's membrane problem

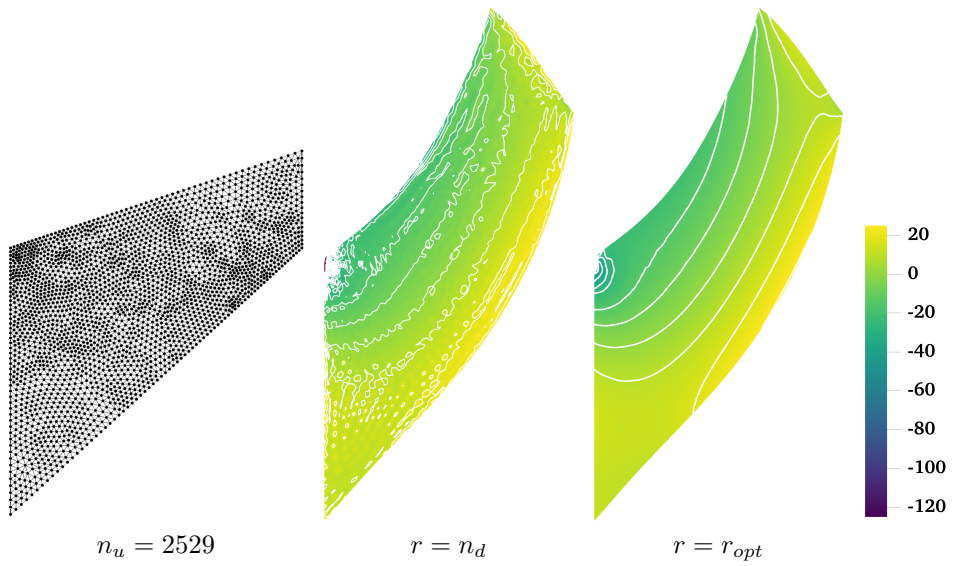


Figure 24: Pressure contour plots for Cook's membrane problem using Tri3–RK

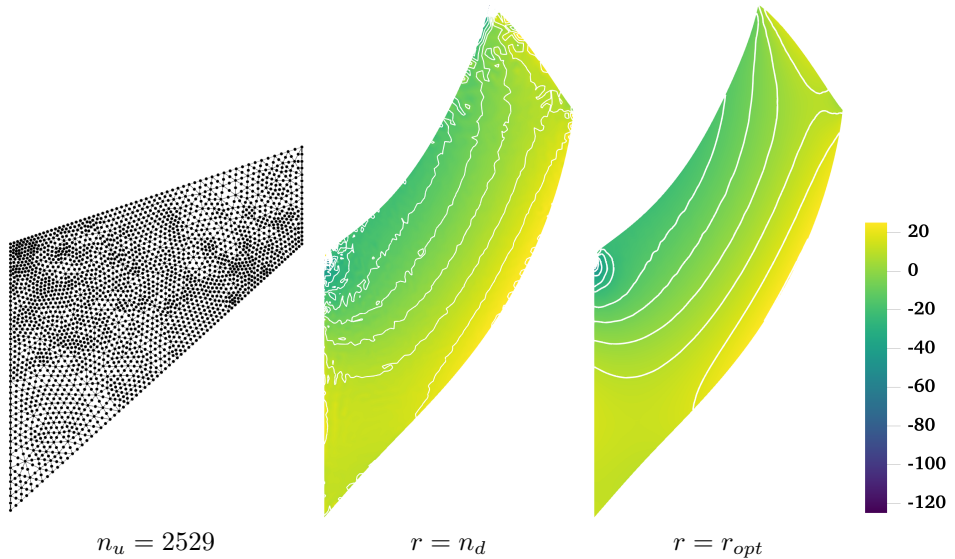


Figure 25: Comparison of pressure contour plots for Cook's membrane problem using Tri6–RK

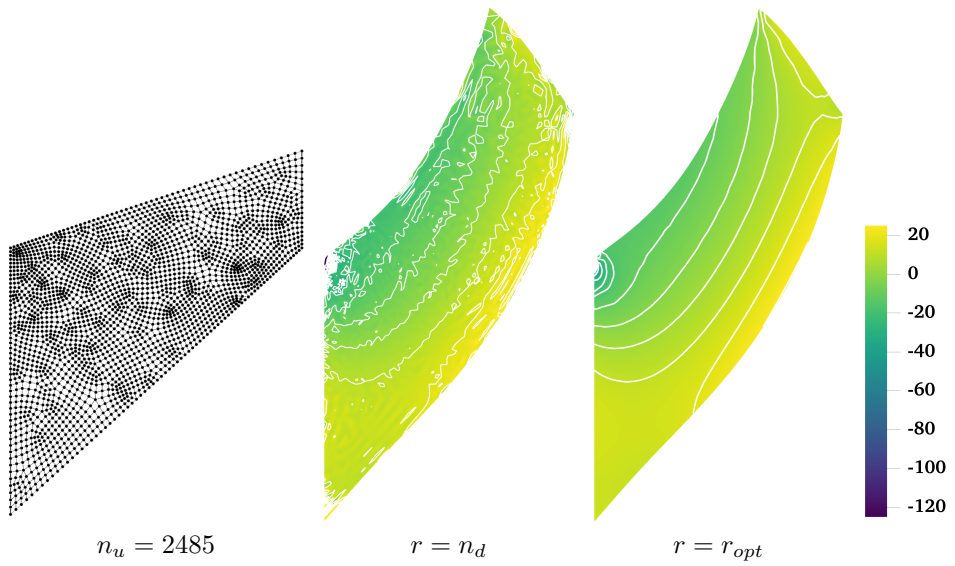


Figure 26: Comparison of pressure contour plots for Cook's membrane problem using Quad4-RK

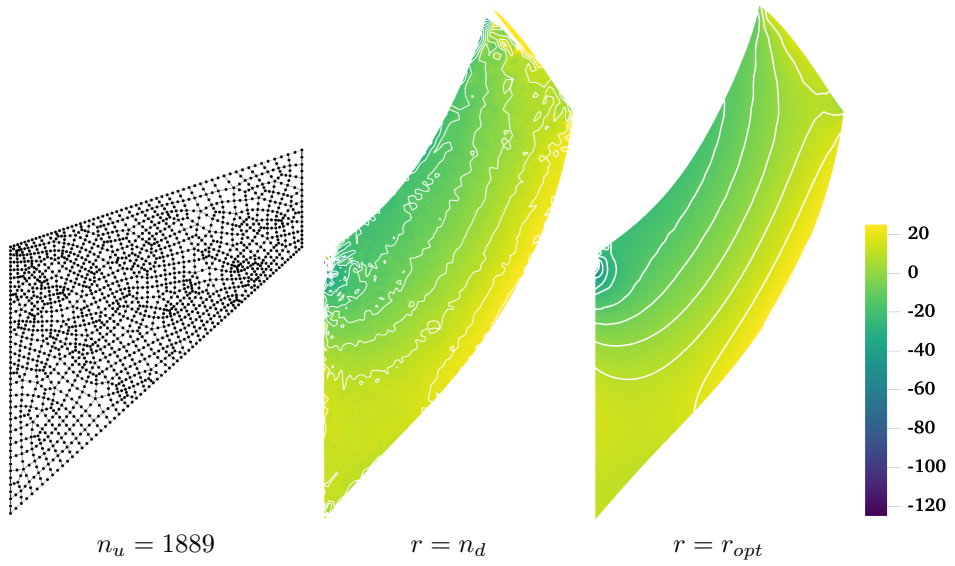


Figure 27: Comparison of pressure contour plots for Cook's membrane problem using Quad8-RK

Table 5: Condition number and efficiency comparison for Cook's membrane problem

Method	Condition number	CPU-time (s) for		
		Shape function	Assembly	Solving
MINI	1.11E06	0.025	0.327	0.022
Tri3-RK($r = n_d$)	1.89E10	1.73	4.160	0.108
Tri3-RK($r = r_{opt}$)	1.13E08	1.290	1.720	0.052
T6P3	1.62E05	0.004	0.380	0.021
Tri6-RK($r = n_d$)	2.48E16	1.62	1.67	0.294
Tri6-RK($r = r_{opt}$)	3.69E10	1.110	0.634	0.077
Q4P1	5.75E12	0.011	0.344	0.021
Quad4-RK($r = n_d$)	5.21E10	2.1	4.89	0.122
Quad4-RK($r = r_{opt}$)	1.97E08	1.5	2.14	0.057
Q8P3	2.69E07	0.005	0.373	0.015
Quad8-RK($r = n_d$)	2.75E15	1.17	1.18	0.184
Quad8-RK($r = r_{opt}$)	8.67E10	0.847	0.471	0.065

5.4. Block under compression problem

The incompressible block problem [62] shown in Figure 28 is considered for testing 3D mixed formulations. The block's dimensions are $2L \times 2L \times L$, $L = 1$. At the center of the top surface of the block is applied a pressure load P with the area of $L \times L$. Due to the symmetry of this problem, only a quarter model is considered. The Young's modulus and Poisson's ratio are set as $E = 240.56839$ and $\nu = 0.5 - 10^{-8}$, respectively.

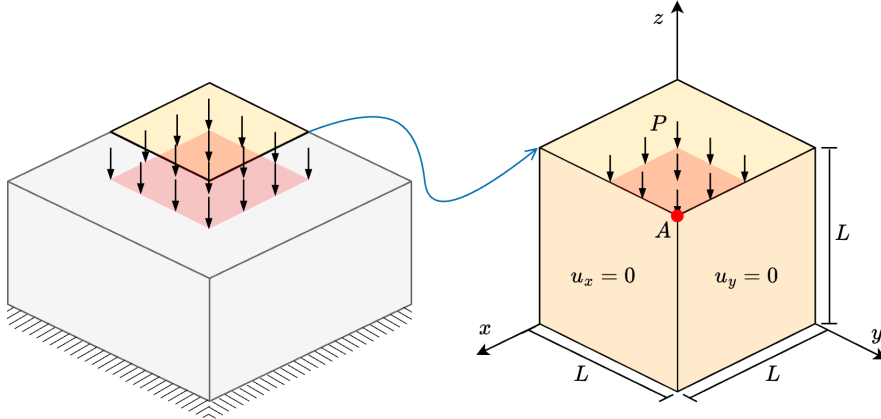


Figure 28: Illustration of block under compression problem

The convergence properties of the mixed formulations are evaluated by comparing the compression level at point A under various loading conditions P/P_0 , where $P_0 = 4$. As shown in Figure 29, all the results exhibit good convergence behavior across different loading levels. Figures 30, 31 study the pressure

508 stability of 3D mixed FE-meshfree formulations, Tet4-RK and Hex8-RK, with
 509 non-uniform nodal distribution, while the pressure is discretized by linear mesh-
 510 free approximations with a characterized support size of 1.5. The corresponding
 511 results also show the well performance of the proposed optimal constraint ratio
 512 $r = r_{opt}$. The mixed formulations with the traditional constraint ratio $r = n_d$
 513 show comparable displacement results, but exhibit significant pressure instabil-
 514 ity.

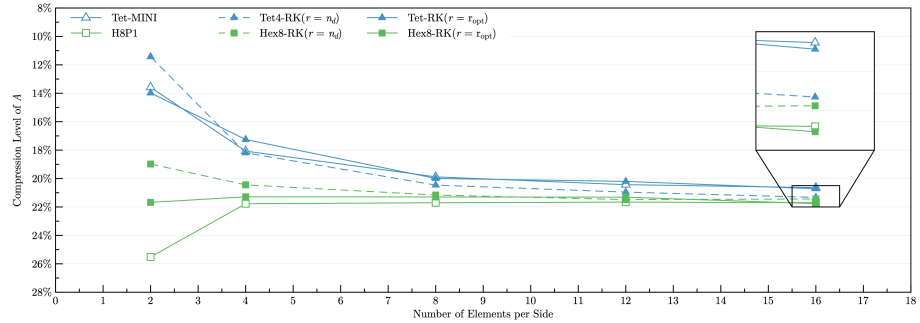


Figure 29: Convergence comparison of compression level (%) at point A for block under compression problem

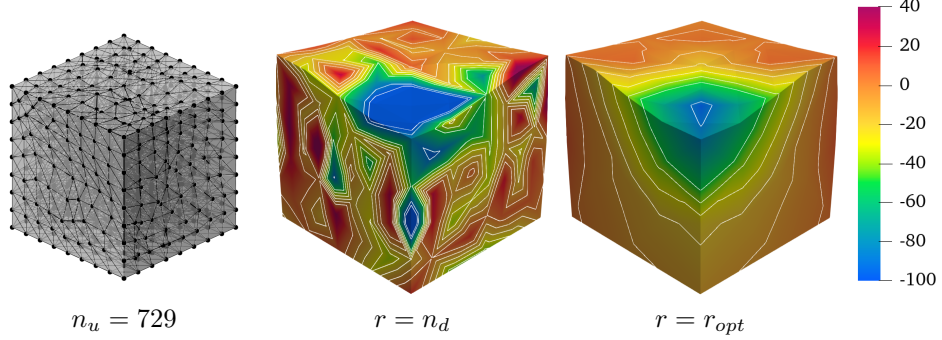


Figure 30: Comparison of pressure contour plots for block under compression problem using Tet4-RK

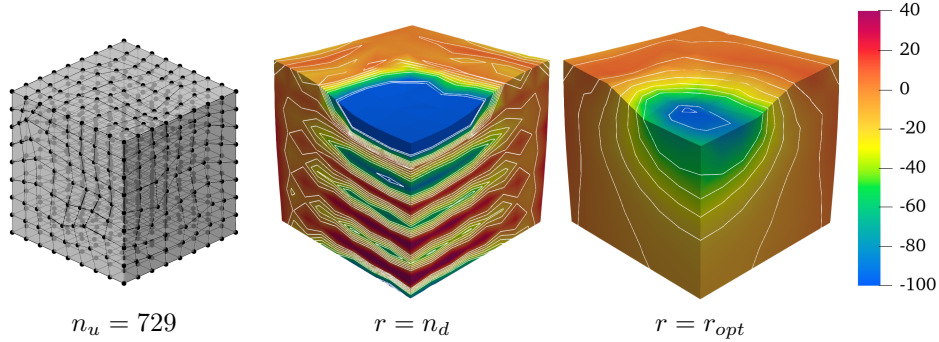


Figure 31: Comparison of pressure contour plots for block under compression problem using Hex8–RK

515 6. Conclusion

516 This paper proposes a novel optimal constraint ratio derived from the inf–sup
 517 condition to address volumetric locking. The optimal constraint ratio requires
 518 that, for a given number of displacement DOFs, the number of pressure DOFs
 519 should remain below a stabilized number determined by the proposed inf–sup
 520 value estimator. For a well-posed nodal distribution, simply counting the dis-
 521 placement and pressure DOFs can determine whether the formulation satisfies
 522 the inf–sup condition. Compared to the traditional constraint ratio, the pro-
 523 posed ratio is theoretically grounded in the inf–sup condition and thus is more
 524 precise.

525 To implement this constraint ratio, a mixed finite element (FE) and meshfree
 526 formulation is developed. Displacements are discretized using 3-node and 6-node
 527 triangular elements, 4-node and 8-node quadrilateral elements in 2D, and 4-node
 528 tetrahedral and 8-node hexahedral elements in 3D. Correspondingly, linear and
 529 quadratic reproducing kernel meshfree approximations are used for pressure
 530 discretization. The reproducing kernel approximation equips globally smooth
 531 shape functions, allowing arbitrary pressure DOF placement without the limit
 532 of element.

533 Inf–sup tests for mixed FE–meshfree formulations with different constraint
 534 ratios verify the effectiveness of the proposed inf–sup value estimator. For effi-
 535 ciency and ease of implementation, the final nodal distribution scheme selects
 536 every other displacement node as a pressure node, ensuring the optimal con-
 537 straint ratio and satisfying the inf–sup condition.

538 A series of 2D and 3D incompressible elasticity examples demonstrate the
 539 effectiveness of the proposed mixed formulation. Results show that formulations
 540 with the optimal constraint ratio yield accurate displacement and pressure solu-
 541 tions. When the constraint ratio exceeds the optimal value, errors rise sharply
 542 to unacceptable levels, with the 8-node quadrilateral element being the only
 543 exception that maintains good displacement accuracy. Error convergence stud-
 544 ies and pressure contour plots further confirm that mixed formulations with

545 the optimal constraint ratio achieve optimal convergence rates and effectively
546 suppress pressure oscillations.

547 **Acknowledgment**

548 The support of this work by the National Natural Science Foundation of
549 China (12102138), the Natural Science Foundation of Fujian Province of China
550 (2023J01108) and the Fundamental Research Funds of Central Universities
551 (ZQN-1014) is gratefully acknowledged.

552 **References**

- 553 [1] F. Brezzi, M. Fortin, Mixed and Hybrid Finite Element Methods, Vol. 15 of
554 Springer Series in Computational Mathematics, Springer, New York, NY,
555 1991.
- 556 [2] T. J. Hughes, The Finite Element Method: Linear Static and Dynamic
557 Finite Element Analysis, Prentice Hall, New Jersey, 2000.
- 558 [3] I. Babuška, R. Narasimhan, The Babuška-Brezzi condition and the patch
559 test: An example, Computer Methods in Applied Mechanics and Engineering
560 140 (1-2) (1997) 183–199.
- 561 [4] K. J. Bathe, Finite Element Procedures, Prentice Hall, Englewood Cliffs,
562 New Jersey, 1996.
- 563 [5] D. S. Malkus, Eigenproblems associated with the discrete LBB condition for
564 incompressible finite elements, International Journal of Engineering Science
565 19 (10) (1981) 1299–1310.
- 566 [6] D. Chapelle, K. J. Bathe, The inf-sup test, Computers & Structures 47 (4)
567 (1993) 537–545.
- 568 [7] F. Brezzi, K. J. Bathe, Studies of finite element procedures the inf-sup
569 condition equivalent forms and applications.
- 570 [8] D. Gallistl, Rayleigh-Ritz approximation of the inf-sup constant for the
571 divergence, Mathematics of Computation 88 (315) (2019) 73–89.
- 572 [9] P. Hood, C. Taylor, Navier-Stokes equations using mixed interpolation,
573 Finite element methods in flow problems (1974) 121–132.
- 574 [10] D. S. Malkus, T. J. Hughes, Mixed finite element methods - Reduced and
575 selective integration techniques: A unification of concepts, Computer Meth-
576 ods in Applied Mechanics and Engineering 15 (1) (1978) 63–81.
- 577 [11] T. Shilt, R. Deshmukh, J. J. McNamara, P. J. O’Hara, Solution of nearly
578 incompressible field problems using a generalized finite element approach,
579 Computer Methods in Applied Mechanics and Engineering 368 (2020)
580 113165.

- 581 [12] J. C. Simo, M. S. Rifai, A class of mixed assumed strain methods and
 582 the method of incompatible modes, International Journal for Numerical
 583 Methods in Engineering 29 (8) (1990) 1595–1638.
- 584 [13] M. Broccardo, M. Micheloni, P. Krysl, Assumed-deformation gradient finite
 585 elements with nodal integration for nearly incompressible large deformation
 586 analysis, International Journal for Numerical Methods in Engineering 78 (9) (2009) 1113–1134.
- 588 [14] W. M. Coombs, T. J. Charlton, M. Cortis, C. E. Augarde, Overcoming vol-
 589 umetric locking in material point methods, Computer Methods in Applied
 590 Mechanics and Engineering 333 (2018) 1–21.
- 591 [15] S. Saloustros, M. Cervera, S. Kim, M. Chiumenti, Accurate and locking-free
 592 analysis of beams, plates and shells using solid elements, Computational
 593 Mechanics 67 (2021) 883–914.
- 594 [16] J. Simo, R. Taylor, K. Pister, Variational and projection methods for the
 595 volume constraint in finite deformation elasto-plasticity, Computer Meth-
 596 ods in Applied Mechanics and Engineering 51 (1-3) (1985) 177–208.
- 597 [17] C. R. Dohrmann, P. B. Bochev, A stabilized finite element method for the
 598 Stokes problem based on polynomial pressure projections, International
 599 Journal for Numerical Methods in Fluids 46 (2) (2004) 183–201.
- 600 [18] A. Valverde-González, J. Reinoso, B. Dortdivanlioglu, M. Paggi, Locking
 601 treatment of penalty-based gradient-enhanced damage formulation for fail-
 602 ure of compressible and nearly incompressible hyperelastic materials, Com-
 603 putational Mechanics 72 (2023) 635–662.
- 604 [19] B.-B. Xu, F. Peng, P. Wriggers, Stabilization-free virtual element method
 605 for finite strain applications, Computer Methods in Applied Mechanics and
 606 Engineering 417 (2023) 116555.
- 607 [20] F. S. Liguori, A. Madeo, S. Marfia, G. Garcea, E. Sacco, A stabilization-
 608 free hybrid virtual element formulation for the accurate analysis of 2D
 609 elasto-plastic problems, Computer Methods in Applied Mechanics and En-
 610 gineering 431 (2024) 117281.
- 611 [21] R. Alves de Sousa, R. Natal Jorge, R. Fontes Valente, J. César de Sá, A new
 612 volumetric and shear locking-free 3D enhanced strain element, Engineering
 613 Computations 20 (7) (2003) 896–925.
- 614 [22] K.-J. Bathe, The inf-sup condition and its evaluation for mixed finite ele-
 615 ment methods, Computers & Structures 79 (2) (2001) 243–252.
- 616 [23] T. J. R. Hughes, Multiscale phenomena: Green's functions, the Dirichlet-
 617 to-Neumann formulation, subgrid scale models, bubbles and the origins of
 618 stabilized methods, Computer Methods in Applied Mechanics and Engi-
 619 neering 127 (1) (1995) 387–401.

- 620 [24] R. Rossi, R. Zorrilla, R. Codina, A stabilised displacement-volumetric
 621 strain formulation for nearly incompressible and anisotropic materials,
 622 Computer Methods in Applied Mechanics and Engineering 377 (2021)
 623 113701.
- 624 [25] E. Karabelas, M. A. F. Gsell, G. Haase, G. Plank, C. M. Augustin, An
 625 accurate, robust, and efficient finite element framework with applications to
 626 anisotropic, nearly and fully incompressible elasticity, Computer Methods
 627 in Applied Mechanics and Engineering 394 (2022) 114887.
- 628 [26] R. Codina, I. Castañar, J. Baiges, Finite element approximation of stabi-
 629 lized mixed models in finite strain hyperelasticity involving displacements
 630 and stresses and/or pressure—An overview of alternatives, International
 631 Journal for Numerical Methods in Engineering (2024) e7540.
- 632 [27] L. Moreno, R. Wuechner, A. Larese, A mixed stabilized MPM formula-
 633 tion for incompressible hyperelastic materials using Variational Subgrid-
 634 Scales, Computer Methods in Applied Mechanics and Engineering 435
 635 (2025) 117621.
- 636 [28] T. J. R. Hughes, L. P. Franca, M. Balestra, A new finite element formu-
 637 lation for computational fluid dynamics: V. Circumventing the babuška-
 638 brezzi condition: A stable Petrov-Galerkin formulation of the stokes prob-
 639 lem accommodating equal-order interpolations, Computer Methods in Ap-
 640 plied Mechanics and Engineering 59 (1) (1986) 85–99.
- 641 [29] A. N. Brooks, T. J. R. Hughes, Streamline upwind/Petrov-Galerkin formu-
 642 lations for convection dominated flows with particular emphasis on the in-
 643 compressible Navier-Stokes equations, Computer Methods in Applied Me-
 644 chanics and Engineering 32 (1) (1982) 199–259.
- 645 [30] L. He, L. Jing, M. Feng, New stabilized mixed finite element methods for
 646 two-field poroelasticity with low permeability, Applied Mathematics and
 647 Computation 494 (2025) 129285.
- 648 [31] D. N. Arnold, F. Brezzi, M. Fortin, A stable finite element for the Stokes
 649 equations, CALCOLO 21 (4) (1984) 337–344.
- 650 [32] F. Auricchio, L. Beirão da Veiga, C. Lovadina, A. Reali, A stability study of
 651 some mixed finite elements for large deformation elasticity problems, Com-
 652 puter Methods in Applied Mechanics and Engineering 194 (9-11) (2005)
 653 1075–1092.
- 654 [33] A. Quarteroni, A. Valli, Numerical Approximation of Partial Differen-
 655 tial Equations, Springer Series in Computational Mathematics, Springer,
 656 Berlin, 1994.
- 657 [34] M. Crouzeix, P. Raviart, Conforming and nonconforming finite ele-
 658 ment methods for solving the stationary Stokes equations I, Revue

- 659 française d'automatique informatique recherche opérationnelle. Mathéma-
 660 tique 7 (R3) (1973) 33–75.
- 661 [35] U. Brink, E. Stein, On some mixed finite element methods for incompress-
 662 ible and nearly incompressible finite elasticity, Computational Mechanics
 663 19 (1) (1996) 105–119.
- 664 [36] T. Belytschko, Y. Y. Lu, L. Gu, Element-free Galerkin methods, Interna-
 665 tional Journal for Numerical Methods in Engineering 37 (2) (1994) 229–256.
- 666 [37] W. K. Liu, S. Jun, Y. F. Zhang, Reproducing kernel particle methods, Interna-
 667 tional Journal for Numerical Methods in Fluids 20 (8-9) (1995) 1081–
 668 1106.
- 669 [38] C. Rodriguez, T.-H. Huang, A variationally consistent reproducing ker-
 670 nel enhanced material point method and its applications to incompressible
 671 materials, Computational Mechanics (2023) 1–20.
- 672 [39] S. W. Chi, J. S. Chen, H. Y. Hu, A weighted collocation on the strong form
 673 with mixed radial basis approximations for incompressible linear elasticity,
 674 Computational Mechanics 53 (2) (2014) 309–324.
- 675 [40] L. Wang, Z. Qian, Y. Zhou, Y. Peng, A weighted meshfree collocation
 676 method for incompressible flows using radial basis functions, Journal of
 677 Computational Physics 401 (2020) 108964.
- 678 [41] A. Ortiz-Bernardin, M. Puso, N. Sukumar, Improved robustness for nearly-
 679 incompressible large deformation meshfree simulations on Delaunay tes-
 680 sellations, Computer Methods in Applied Mechanics and Engineering 293
 681 (2015) 348–374.
- 682 [42] T. J. Hughes, J. A. Cottrell, Y. Bazilevs, Isogeometric analysis: CAD,
 683 finite elements, NURBS, exact geometry and mesh refinement, Computer
 684 Methods in Applied Mechanics and Engineering 194 (39-41) (2005) 4135–
 685 4195.
- 686 [43] F. Auricchio, L. Beirão da Veiga, C. Lovadina, A. Reali, The importance
 687 of the exact satisfaction of the incompressibility constraint in nonlinear
 688 elasticity: Mixed FEMs versus NURBS-based approximations, Computer
 689 Methods in Applied Mechanics and Engineering 199 (5) (2010) 314–323.
- 690 [44] A. Huerta, S. Fernández-Méndez, Locking in the incompressible limit for
 691 the element-free Galerkin method, International Journal for Numerical
 692 Methods in Engineering 51 (11) (2001) 1361–1383.
- 693 [45] J. Dolbow, T. Belytschko, Volumetric locking in the element free Galerkin
 694 method, International Journal for Numerical Methods in Engineering 46 (6)
 695 (1999) 925–942.

- 696 [46] G. Moutsanidis, J. J. Koester, M. R. Tupek, J.-S. Chen, Y. Bazilevs, Treatment
 697 of near-incompressibility in meshfree and immersed-particle methods,
 698 *Computational Particle Mechanics* 7 (2) (2020) 309–327.
- 699 [47] G. Moutsanidis, W. Li, Y. Bazilevs, Reduced quadrature for FEM, IGA
 700 and meshfree methods, *Computer Methods in Applied Mechanics and En-*
 701 *gineering* 373 (2021) 113521.
- 702 [48] Z.-Y. Wang, Y.-F. Jin, Z.-Y. Yin, Y.-Z. Wang, Overcoming volumetric
 703 locking in stable node-based smoothed particle finite element method with
 704 cubic bubble function and selective integration, *International Journal for*
 705 *Numerical Methods in Engineering* 123 (24) (2022) 6148–6169.
- 706 [49] T. Elguedj, Y. Bazilevs, V. Calo, T. Hughes, B^- and F^- projection meth-
 707 ods for nearly incompressible linear and non-linear elasticity and plasticity
 708 using higher-order NURBS elements, *Computer Methods in Applied Me-*
 709 *chanics and Engineering* 197 (33-40) (2008) 2732–2762.
- 710 [50] J. S. Chen, S. Yoon, H. P. Wang, W. K. Liu, An improved reproducing
 711 kernel particle method for nearly incompressible finite elasticity, *Computer*
 712 *Methods in Applied Mechanics and Engineering* 181 (1) (2000) 117–145.
- 713 [51] C. M. Goh, P. M. F. Nielsen, M. P. Nash, A stabilised mixed mesh-
 714 free method for incompressible media: Application to linear elasticity and
 715 Stokes flow, *Computer Methods in Applied Mechanics and Engineering* 329
 716 (2018) 575–598.
- 717 [52] D. S. Bombarde, M. Agrawal, S. S. Gautam, A. Nandy, Hellinger–Reissner
 718 principle based stress–displacement formulation for three-dimensional iso-
 719 geometric analysis in linear elasticity, *Computer Methods in Applied Me-*
 720 *chanics and Engineering* 394 (2022) 114920.
- 721 [53] H. Casquero, M. Golestanian, Vanquishing volumetric locking in quadratic
 722 NURBS-based discretizations of nearly-incompressible linear elasticity:
 723 CAS elements, *Computational Mechanics* 73 (6) (2024) 1241–1252.
- 724 [54] A. Huerta, Y. Vidal, P. Villon, Pseudo-divergence-free element free
 725 Galerkin method for incompressible fluid flow, *Computer Methods in Ap-*
 726 *plied Mechanics and Engineering* 193 (12-14) (2004) 1119–1136.
- 727 [55] C. T. Wu, W. Hu, J. S. Chen, A meshfree-enriched finite element method
 728 for compressible and near-incompressible elasticity, *International Journal*
 729 *for Numerical Methods in Engineering* 90 (7) (2012) 882–914.
- 730 [56] T. Vu-Huu, C. Le-Thanh, H. Nguyen-Xuan, M. Abdel-Wahab, A high-
 731 order mixed polygonal finite element for incompressible Stokes flow analy-
 732 sis, *Computer Methods in Applied Mechanics and Engineering* 356 (2019)
 733 175–198.

- 734 [57] E. Stein, R. de Borst, T. J. R. Hughes (Eds.), Encyclopedia of Computational Mechanics, John Wiley, Chichester, West Sussex, 2004.
- 735
- 736 [58] I. Babuška, J. Osborn, Eigenvalue Problems, in: Handbook of Numerical Analysis, Vol. 2 of Finite Element Methods (Part 1), Elsevier, 1991, pp. 641–787.
- 737
- 738
- 739 [59] K. Yosida, Functional Analysis, 6th Edition, Classics in Mathematics, Springer-Verlag, Berlin Heidelberg, 1995.
- 740
- 741 [60] J. Wu, D. Wang, An accuracy analysis of Galerkin meshfree methods accounting for numerical integration, Computer Methods in Applied Mechanics and Engineering 375 (2021) 113631.
- 742
- 743
- 744 [61] S. Timoshenko, J. Goodier, Theory of Elasticity, Engineering Mechanics Series, McGraw-Hill, 1969.
- 745
- 746 [62] S. Reese, P. Wriggers, B. D. Reddy, A new locking-free brick element technique for large deformation problems in elasticity, Computers & Structures 75 (3) (2000) 291–304.
- 747
- 748
- 749 [63] S. C. Brenner, L. R. Scott, The Mathematical Theory of Finite Element Methods, Springer, New York, 2008.
- 750

751 **Appendix A. Error estimator for mixed-formulation**

752 In this appendix, the traditional error estimators for mixed-formulation are
 753 illustrated herein, the proof is referred to [63]. For incompressible elasticity
 754 problems, i.e. $\kappa \rightarrow \infty$, $c(q, p) = 0$, the weak formula of Eq. (14) is rewritten as:
 755 Find $\mathbf{u}_h \in V_h, p_h \in Q_h$,

$$\begin{aligned} a(\mathbf{v}_h, \mathbf{u}_h) + b(\mathbf{v}_h, p_h) &= f(\mathbf{v}_h), & \forall \mathbf{v}_h \in V_h \\ b(\mathbf{u}_h, q_h) &= 0, & \forall q_h \in Q_h \end{aligned} \quad (\text{A.1})$$

756 According to the definition of bilinear form b in Eq. (10), for a $\mathbf{u}_h \in \ker \mathcal{P}_h$, then
 757 the second equation of Eq. (A.1) is naturally satisfied. Thus, the above weak
 758 formulation can be equivalently split into the following two steps: Firstly, find
 759 $\mathbf{u}_h \in \ker \mathcal{P}_h$,

$$a(\mathbf{v}_h, \mathbf{u}_h) = f(\mathbf{v}_h), \quad \forall \mathbf{v}_h \in \ker \mathcal{P}_h \quad (\text{A.2})$$

760 After determine \mathbf{u}_h , then find $p_h \in Q_h$,

$$b(\mathbf{v}_h, p_h) = f(\mathbf{v}_h) - a(\mathbf{v}_h, \mathbf{u}_h), \quad \forall \mathbf{v}_h \in V_h \quad (\text{A.3})$$

761 To further analyze the error of mixed-formulation, the following properties
 762 of bilinear forms a and b should be defined [63]:

763 • **Continuity:**

$$a(\mathbf{v}, \mathbf{u}) \leq C_a \|\mathbf{v}\|_V \|\mathbf{u}\|_V, \quad \forall \mathbf{v}, \mathbf{u} \in V \quad (\text{A.4})$$

$$b(\mathbf{v}, q) \leq C_b \|\mathbf{v}\|_V \|q\|_Q, \quad \forall \mathbf{v} \in V, \forall q \in Q \quad (\text{A.5})$$

764 • **Coercivity:**

$$\|\mathbf{v}\|_V \leq \frac{1}{\alpha} \sup_{\mathbf{w} \in V} \frac{|a(\mathbf{v}, \mathbf{w})|}{\|\mathbf{w}\|_V}, \quad \forall \mathbf{v} \in V \quad (\text{A.6})$$

765 • **Inf-sup condition:**

$$\|q\|_Q \leq \frac{1}{\beta} \sup_{\mathbf{v} \in V} \frac{|b(\mathbf{v}, q)|}{\|\mathbf{v}\|_V}, \quad \forall q \in Q \quad (\text{A.7})$$

766 where C_a and C_b are positive constants independent of mesh size h . α and β
 767 are the coercivity and inf-sup constants, respectively, which will influence the
 768 accuracy of mixed-formulation.

769 For the error of displacement, the Céa's Theorem used for the error analysis
 770 of traditional Galerkin formulation is not always valid for mixed-formulation.
 771 This is because most of mixed-formulation can not ensure $\ker \mathcal{P}_h \subset \ker \mathcal{P}$ to
 772 maintain the orthogonality of bilinear form a that is required in the proof of
 773 Céa's Theorem. So we first introduce the following error estimator for displacement
 774 in the case of $\ker \mathcal{P}_h \not\subset \ker \mathcal{P}$. For any $\mathbf{v}_h \in \ker \mathcal{P}_h$, considering the triangle

775 inequality, the coercivity in Eq. (A.6) and the continuity in Eq. (A.4), we have:

$$\begin{aligned}
\|\mathbf{u} - \mathbf{u}_h\|_V &\leq \|\mathbf{u} - \mathbf{v}_h\|_V + \|\mathbf{v}_h - \mathbf{u}_h\|_V \\
&\leq \|\mathbf{u} - \mathbf{v}_h\|_V + \frac{1}{\alpha} \sup_{\mathbf{w}_h \in \ker \mathcal{P}_h} \frac{|a(\mathbf{v}_h - \mathbf{u}_h, \mathbf{w}_h)|}{\|\mathbf{w}_h\|_V} \\
&\leq \|\mathbf{u} - \mathbf{v}_h\|_V + \frac{1}{\alpha} \sup_{\mathbf{w}_h \in \ker \mathcal{P}_h} \frac{|a(\mathbf{v}_h - \mathbf{u}, \mathbf{w}_h)| + |a(\mathbf{u} - \mathbf{u}_h, \mathbf{w}_h)|}{\|\mathbf{w}_h\|_V} \\
&\leq (1 + \frac{C}{\alpha}) \|\mathbf{u} - \mathbf{v}_h\|_V + \frac{1}{\alpha} \sup_{\mathbf{w}_h \in \ker \mathcal{P}_h} \frac{|a(\mathbf{u} - \mathbf{u}_h, \mathbf{w}_h)|}{\|\mathbf{w}_h\|_V}
\end{aligned} \tag{A.8}$$

776 According to Eqs. (A.2), (A.3) and continuity in Eq. (A.5), the second term on
777 the right hand side of above equation can be rewritten as:

$$\begin{aligned}
\sup_{\mathbf{w}_h \in \ker \mathcal{P}_h} \frac{|a(\mathbf{u} - \mathbf{u}_h, \mathbf{w}_h)|}{\|\mathbf{w}_h\|_V} &= \sup_{\mathbf{w}_h \in \ker \mathcal{P}_h} \frac{|a(\mathbf{u}, \mathbf{w}_h) - f(\mathbf{w}_h)|}{\|\mathbf{w}_h\|_V} \\
&= \sup_{\mathbf{w}_h \in \ker \mathcal{P}_h} \frac{|b(\mathbf{w}_h, p)|}{\|\mathbf{w}_h\|_V} \\
&= \sup_{\mathbf{w}_h \in \ker \mathcal{P}_h} \frac{|b(\mathbf{w}_h, p - q_h)|}{\|\mathbf{w}_h\|_V} \\
&\leq C_b \|p - q_h\|_Q
\end{aligned} \tag{A.9}$$

778 where q_h is an arbitrary variable in Q_h . Combining the Eqs. (A.8) and (A.9),
779 the following error estimator for displacement can be obtained:

$$\|\mathbf{u} - \mathbf{u}_h\|_V \leq (1 + \frac{C_a}{\alpha}) \inf_{\mathbf{v}_h \in \ker \mathcal{P}_h} \|\mathbf{u} - \mathbf{v}_h\|_V + \frac{C_b}{\alpha} \inf_{q_h \in Q_h} \|p - q_h\|_Q \tag{A.10}$$

780 Furthermore, for the error estimator of pressure, according to the first equa-
781 tion of Eq. (6) and $V_h \subset V$, we have:

$$b(\mathbf{v}_h, p) = f(\mathbf{v}_h) - a(\mathbf{v}_h, \mathbf{u}), \quad \forall \mathbf{v}_h \in V_h \tag{A.11}$$

782 and then subtracting Eq. (A.11) from Eq. (A.3) yields:

$$b(\mathbf{v}_h, p - p_h) = -a(\mathbf{v}_h, \mathbf{u} - \mathbf{u}_h), \quad \forall \mathbf{v}_h \in V_h \tag{A.12}$$

783 In this context, for any $q_h \in Q_h$, invoking the triangle inequality, Eqs. (A.7)
784 and (A.5) leads to:

$$\begin{aligned}
\|p - p_h\|_Q &\leq \|p - q_h\|_Q + \|q_h - p_h\|_Q \\
&\leq \|p - q_h\|_Q + \frac{1}{\beta} \sup_{\mathbf{v} \in V_h} \frac{|b(\mathbf{v}_h, q_h - p_h)|}{\|\mathbf{v}_h\|_V} \\
&\leq \|p - q_h\|_Q + \frac{1}{\beta} \sup_{\mathbf{v} \in V_h} \frac{|a(\mathbf{v}_h, \mathbf{u} - \mathbf{u}_h)| + |b(\mathbf{v}_h, p - q_h)|}{\|\mathbf{v}_h\|_V} \\
&\leq \frac{C_a}{\beta} \|\mathbf{u} - \mathbf{u}_h\|_V + (1 + \frac{C_b}{\beta}) \|p - q_h\|_Q
\end{aligned} \tag{A.13}$$

785 Consequently, the error estimator for pressure can be given by:

$$\|p - p_h\|_Q \leq \frac{C_a}{\beta} \|\mathbf{u} - \mathbf{u}_h\|_V + \left(1 + \frac{C_b}{\beta}\right) \inf_{q_h \in Q_h} \|p - q_h\|_Q \quad (\text{A.14})$$

786 Obviously, the error estimators of Eqs. (A.10) and (A.14) are both related
 787 to the coercivity constant α , inf-sup constant β and the approximability of
 788 spaces $\ker \mathcal{P}_h$, Q_h , in which the approximability is usually measured by the
 789 interpolation error of approximation method. However, the approximability
 790 of space $\ker \mathcal{P}_h$ is not trivial to be evaluated directly. To further evaluate the
 791 approximability of space $\ker \mathcal{P}_h$, let a variable $\mathbf{w}_h \in V_h \setminus \ker \mathcal{P}_h$ to satisfy the
 792 following relationship:

$$\inf_{\bar{\mathbf{v}}_h \in \ker \mathcal{P}_h} \|\mathbf{u} - (\bar{\mathbf{v}}_h + \mathbf{w}_h)\|_V = \inf_{\mathbf{v}_h \in V_h} \|\mathbf{u} - \mathbf{v}_h\|_V \quad (\text{A.15})$$

793 such that the approximability of space $\ker \mathcal{P}_h$ can be transformed to that of
 794 space V_h that is easy to be measured. If $\mathbf{w}_h = \mathbf{0}$, $\ker \mathcal{P}_h$ has the identical
 795 approximability with V_h :

$$\inf_{\bar{\mathbf{v}}_h \in \ker \mathcal{P}_h} \|\mathbf{u} - \bar{\mathbf{v}}_h\|_V = \inf_{\mathbf{v}_h \in V_h} \|\mathbf{u} - \mathbf{v}_h\|_V \quad (\text{A.16})$$

796 If $\mathbf{w}_h \neq \mathbf{0}$, leading a triangle inequality we have:

$$\|\mathbf{u} - \bar{\mathbf{v}}_h\|_V \leq \|\mathbf{u} - (\bar{\mathbf{v}}_h + \mathbf{w}_h)\|_V + \|\mathbf{w}_h\|_V \quad (\text{A.17})$$

797 where, reconsidering the Eq. (26) in Lemma 1, as $\mathbf{w}_h \in V_h \setminus \ker \mathcal{P}_h$ and $\mathbf{w}_h \neq \mathbf{0}$,
 798 the following relation can be obtained:

$$\|\mathbf{w}_h\|_V \leq \frac{1}{\beta} \|\mathcal{P}_h \mathbf{w}_h\|_Q \quad (\text{A.18})$$

799 where, using Eqs. (25), (17) and considering $\mathbf{u} \in \ker \mathcal{P}$, $\bar{\mathbf{v}}_h \in \ker \mathcal{P}_h$, the right
 800 hand side of above equation can further be transformed as follows:

$$\begin{aligned} \|\mathcal{P}_h \mathbf{w}_h\|_Q &= \sup_{q_h \in Q_h} \frac{|\frac{1}{\kappa}(\mathcal{P}_h \mathbf{w}_h, q_h)|}{\|q_h\|_Q} = \sup_{q_h \in Q_h} \frac{|b(\mathbf{w}_h, q_h)|}{\|q_h\|_Q} \\ &= \sup_{q_h \in Q_h} \frac{|b(\mathbf{u} - (\mathbf{w}_h + \bar{\mathbf{v}}_h), q_h)|}{\|q_h\|_Q} \\ &\leq C_b \|\mathbf{u} - (\mathbf{w}_h + \bar{\mathbf{v}}_h)\|_V \end{aligned} \quad (\text{A.19})$$

801 With the combination of Eqs. (A.17), (A.18) and (A.19), the approximability
 802 of $\ker \mathcal{P}_h$ for the case of $\mathbf{w}_h \neq \mathbf{0}$ is given by:

$$\inf_{\bar{\mathbf{v}}_h \in \ker \mathcal{P}_h} \|\mathbf{u} - \bar{\mathbf{v}}_h\|_V \leq \left(1 + \frac{C_b}{\beta}\right) \inf_{\mathbf{v}_h \in V_h} \|\mathbf{u} - \mathbf{v}_h\|_V \quad (\text{A.20})$$